
This manuscript is a preprint and has been formally accepted for publication in *Basin Research*. The final version of this manuscript will be available via the 'Peer-reviewed Publication DOI' link on the right-hand side of this webpage. We welcome feedback, so please feel free to contact any of the authors directly or by leaving a comment.

1 The geometric and temporal evolution of fault-related folds
2 constrains normal fault growth patterns, Barents Sea, offshore
3 Norway

4 Ahmed Alghuraybi^{1*}, Rebecca E. Bell¹, Christopher A-L. Jackson²

5
6
7 ¹*Basins Research Group (BRG), Earth Science and Engineering, Imperial College, Prince Consort*
8 *Road, London, SW7 2BP, UK*

9
10 ²*Department of Earth, Atmospheric and Environmental Sciences, The University of Manchester,*
11 *Williamson Building, Oxford Road, Manchester, M13 9PL, UK*

12
13 *Corresponding author: Ahmed Alghuraybi (a.alghuraybi19@imperial.ac.uk)

14

15 Acknowledgement

16 The results presented here are part of Ahmed Alghuraybi's PhD research at Imperial College
17 London, funded by Saudi Aramco. We thank the Norwegian Petroleum Directorate (NPD) for
18 making the seismic and well data publicly available on the Norwegian national data repository
19 for petroleum data (NDR). The Fruholmen 3D seismic reflection dataset can be downloaded from
20 the Diskos NDR (<https://portal.diskos.cgg.com/whereoil-data/>) by searching for "Fruholmen 3D"
21 and the well data can be found by searching for "7124/4-1 S". We thank Schlumberger for
22 providing access to Petrel software and Geoteric for access to their software. We also thank Amir
23 Joffe, Bailey Lathrop, and Sophie Pan from Imperial College's Basins Research Group (BRG) for
24 their input and helpful discussions throughout this research. The authors extend their thanks to
25 Hongdan Deng, John Conneally and Giovanni Camanni for their constructive reviews that helped
26 improve the initial version of this paper. The journal editor-in-chief Atle Rotevatn and the entire

27 Basin Research editorial staff are thanked for editorial handling and assistance with paper
28 production.

29

30 Data Availability Statement

31 The data that support the findings of this study are openly available in Norwegian national data
32 repository for petroleum data at <https://portal.diskos.cgg.com/whereoil-data/>.

33

34 Abstract

35 Extensional growth folds form ahead of the tips of propagating normal faults. These folds can
36 accommodate a considerable amount of extensional strain and they may control rift geometry.

37 Fold-related surface deformation may also control the sedimentary evolution of syn-rift
38 depositional systems. Thus, by examining the stratigraphic record, we can constrain the four-

39 dimensional evolution of extensional growth folds, which in turn provides a record of fault
40 growth and broader rift history. Here we use high-quality 3D seismic reflection and borehole data

41 from the SW Barents Sea, offshore northern Norway to determine the geometric and temporal
42 evolution of extensional growth folds associated with a large, long-lived, basement-rooted fault.

43 We show that the fault grew via the linkage of four segments, and that fault growth was
44 associated with the formation of fault-parallel and fault-perpendicular folds that accommodated

45 a substantial portion (10 – 40%) of the total extensional strain. Several periods of fault-
46 propagation folding occurred in response to periodic burial of the fault, with individual folding

47 events (c. 25 Myr and 32 Myr) lasting a considered part of the c. 130 Myr rift period. Our study
48 supports previous suggestions that continuous (i.e., folding) as well as discontinuous (i.e.,

49 faulting) deformation must be explicitly considered when assessing total strain in extensional
50 setting. We also show that changes in the architecture of growth strata record alternating periods
51 of folding and faulting, and that the margins of rift-related depocentres may be characterised by
52 basinward-dipping monoclines as opposed to fault-bound scarps. Our findings have broader
53 implications for our understanding of the structural, physiographic, and tectonostratigraphic
54 evolution of rift basins.

55 *Key words: Normal Fault Growth, Extensional Growth Folds, Continuous Strain, Strike-Projections*
56 *, Barents Sea*

57

58 Introduction

59 Basin-bounding normal fault systems have a complex three-dimensional geometry, consisting of
60 variably linked or unlinked segments that branch along both the strike and dip directions (e.g.
61 Walsh et al., 1999, 2002, 2003; Childs et al., 2002; van der Zee & Urai, 2005; Schöpfer et al., 2006;
62 Long & Imber, 2010; Giba et al., 2012; Jackson & Rotevatn, 2013; Fossen & Rotevatn, 2016;
63 Freitag et al., 2017; Camanni et al., 2019; Deng & McClay, 2021; Roche et al. 2021). These
64 geometries reflect the fact that these systems evolve via the growth, interaction, and linkage of
65 smaller segments (e.g. Jackson, 1987; Schlische, 1992; Morley, 1999; Gawthorpe & Leeder, 2000;
66 McLeod et al., 2000; Peacock, 2002). Therefore, how faults grow has significant implications for
67 the structural, physiographic, and tectonostratigraphic evolution of rift basins, as well as their
68 potential for hosting energy resources and for sequestering CO₂ (e.g. Gawthorpe & Leeder, 2000;
69 Childs et al., 2017; Jackson et al., 2017; Michie et al., 2021).

70 Fault growth patterns also control the development of growth folds, which are also known as
71 fault-propagation folds. These structures form ahead of the propagating normal fault tips and
72 typically form during the early phases of extension, during which time they may accommodate a
73 considerable amount of extensional strain (e.g. Withjack et al., 1990; Allmendinger, 1998;
74 Cosgrove & Ameen, 1999; Hardy & McClay, 1999; Gawthorpe & Leeder, 2000; Withjack &
75 Callaway, 2000; Coleman et al., 2019; Jackson et al., 2020). fault-propagation folds play a major
76 role in controlling rift geometry and the sedimentary evolution of syn-rift systems as they alter
77 sediment-transport pathways and may act as sediment sources if eroded (e.g. Laubscher, 1982;
78 Maurin & Niviere, 1999; Gawthorpe & Leeder, 2000; Sharp et al., 2000; Lewis et al., 2015; Jackson
79 & Lewis, 2016; Coleman et al., 2019). Geometrically complex hanging wall fold and fault
80 geometries can develop within a single regional extensional stress regime (e.g. Khalil & McClay,
81 2018), although multiphase extension, stratigraphic and rheological variability in the host rock,
82 and temporal and spatial changes in regional stress regime can all result in additional, four-
83 dimensionally complexity (e.g. Schöpfer et al., 2007; Conneally et al., 2017; Deng & McClay,
84 2019; Jackson et al., 2020). For example, along-strike variations in displacement along segmented
85 normal faults may mean that breached and un-breached growth folds are spatially and
86 temporally related (e.g. Gawthorpe et al., 1997; Gupta et al., 1999; Corfield & Sharp, 2000; Sharp
87 et al., 2000; Corfield et al., 2001; Khalil & McClay, 2002; Willsey et al., 2002; White & Crider, 2006;
88 Lewis et al., 2013; Lewis et al., 2015; Khalil & McClay, 2017; Coleman et al., 2019; Jackson et al.,
89 2020). These structural dynamics are often recorded in the stratigraphic architecture of and
90 facies distributions within fault- and fold-bound hanging wall depocenters (Gawthorpe et al.,
91 1997; Corfield & Sharp, 2000; Sharp et al., 2000; Kane et al., 2010; Duffy et al., 2013; Coleman et

92 al., 2019). Fault-propagation folds also vary in shape and size across the fault surface as a function
93 of, for example, the depth at which faults nucleate, changes in host rock lithology and rheology,
94 dip linkage between initially isolated segments, and spatial changes in fault dip (e.g. Mansfield &
95 Cartwright, 2000; Rykkelid & Fossen, 2002). Despite containing a record of fault growth and
96 broader rift history, few studies have attempted to analyse fault-propagation folds in four
97 dimensions using borehole and 3D seismic reflection data (e.g. Gawthorpe et al., 1997; Corfield
98 et al., 2001; Patton, 2004; Lewis et al., 2015; Coleman et al., 2019; McHarg et al., 2020; Long &
99 Imber, 2010; Conneally et al., 2017; Deng & McClay, 2019). Such data are optimal for this
100 purpose, given they reveal the present basin structure and stratigraphic architecture, and allow
101 inferences to be made regarding the underlying kinematics.

102 In this study we use high-quality 3D seismic reflection and borehole data from the SW Barents
103 Sea, offshore northern Norway to provide a detailed analysis of the geometric and temporal
104 evolution of fault-propagation folding associated with part of a large, basement-rooted fault that
105 is c. 30 km long, c. 5 km tall , and that has up to 2 km of displacement. This fault forms part of the
106 Troms-Finnmark Fault Complex (TFFC), a basement-rooted, rift-related structure that
107 accommodated several phases of Palaeozoic to Cenozoic extension (e.g. Gabrielsen, 1984;
108 Indrevær et al., 2013). Combining both 3D seismic reflection and borehole data enables us to
109 study the temporal evolution of this fault system using age-constrained synkinematic
110 stratigraphy. By doing this we show how large, crustal-scale faults, and their associated folds,
111 evolve and control rift structure and sedimentation over timescales of c. 100 Myr.

112

113 Geological Setting

114 Regional Tectonics

115 The Barents Sea is a shallow continental shelf located in the northwest corner of the Eurasian
116 tectonic plate, between the Arctic Ocean to the north and the Russian and Norwegian coastlines
117 to the south (Gabrielsen, 1984) (Fig. 1). The SW Barents Sea is presently a passive margin that
118 consists of numerous predominately NNE-trending rift basins (e.g. Nordkapp Basin (NB),
119 Hammerfest Basin (HB), and Sørvestsnaget Basin (SB); Fig. 1a) and basement highs (e.g. Fedynsky
120 High (FH), Loppa High (LH), and Stappen High (SH); Fig. 1a) (Faleide et al., 1984, 1993, 2008).
121 Multiple phases of rifting occurred in the Barents Sea, initiating in the Devonian in response to
122 the collapse of the Caledonian orogenic belt, and concluding with the opening of the Norwegian
123 and Greenland seas and the onset of seafloor spreading in the Eocene (Faleide et al., 1984, 1993,
124 2008; Gabrielsen, 1984; Gabrielsen et al., 2016). The late Cambrian to mid-Devonian Caledonian
125 Orogeny deformed the crystalline basement rocks of the SW Barents Sea (Faleide et al., 1984).
126 The large-scale fabric of these Caledonian igneous and metamorphic rocks played a major role in
127 shaping the evolution and present structural framework of the area (see below; e.g., Faleide et
128 al., 1984; Ritzmann & Faleide, 2007).

129 Seismic reflection and wide-angle refraction data, and potential field (e.g., gravity and magnetic)
130 data indicate that at least four distinct rift phases controlled the long-term evolution and large-
131 scale structure of the SW Barents Sea (Gabrielsen et al., 1984; Faleide et al., 1993).

132 . These rift phases occurred in the Late Devonian – Carboniferous , Late Permian, Middle Jurassic
133 – Early Cretaceous, and Paleocene – Eocene (Faleide et al., 2008). Crustal extension in the Late
134 Devonian – Carboniferous created N- to NE-trending half-grabens and resulted in the formation
135 of the TFFC (e.g. Gabrielsen, 1984; Faleide et al., 2008; Indrevær et al., 2013). The TFFC is a
136 basement-rooted normal fault system that represents a major structural element of the SW
137 Barents Sea, separating recent shelf sediments offshore from onshore crystalline basement rocks
138 (e.g. Gabrielsen, 1984; Indrevær et al., 2013). The TFFC runs parallel to the present-day coastline
139 of Norway, striking NE-SW in its southernmost part and NW-SE in its northern part (Gabrielsen,
140 1984). Previous studies of the TFFC suggest that it was continually reactivated until the Eocene
141 (Gabrielsen et al., 1984; Faleide et al., 1993).

142 In the latest Carboniferous to Permian and following the first phase of rifting, the newly formed
143 narrow basins were filled with evaporites and carbonates, which were later covered by clastic
144 rocks (Faleide et al., 1984). Clastic sedimentation continued during the second phase of rifting in
145 the Late Permian, which created considerable accommodation (e.g. Johansen et al., 1993;
146 Larssen et al., 2002). The Triassic was a period of moderate tectonic activity that saw high rates
147 of subsidence and clastic sediment accumulation , which ended with a regional marine
148 transgression (e.g. Glørstad-Clark et al., 2010; Harishidayat et al., 2015; Mattos et al., 2016).

149 During the Middle Jurassic – Early Cretaceous, a third, intense phase of rifting occurred in the SW
150 Barents Sea, resulting in the formation of multiple large basins bounded by basement-cored
151 structural highs (e.g. Gabrielsen, 1984; Doré, 1995; Mattos et al., 2016). This third phase of rifting
152 was also marked by notable across-fault thickening of clastic (growth) strata (Faleide et al., 1993;

153 2008). The base of the Cenozoic succession is marked by a regional unconformity that separates
154 Cretaceous and Paleogene strata (Faleide et al., 2008). The fourth and last reported rifting phase
155 in the Palaeocene – Eocene is linked to the opening of the Norwegian and Greenland seas (e.g.
156 Eldholm & Thiede, 1980; Faleide et al., 2008; Harishidayat et al., 2015). This phase of rifting
157 coincided with increased magmatic activity, followed by a period of glaciation, uplift and erosion
158 (e.g. Eldholm & Thiede, 1980; Faleide et al., 2008; Harishidayat et al., 2015).

159

160 Stratigraphy

161 The sediments filling the SW Barents Sea basins are dominated by clastic rocks overlying
162 Caledonian crystalline basement (e.g. Doré, 1995; Harishidayat et al., 2015) (Fig. 2). The clastic-
163 dominated succession can be divided into six megasequences (e.g. Glørstad-Clark et al., 2010).
164 The 1st megasequence comprises Late Devonian-Early Carboniferous fluvial deposits at its base
165 and marginal marine deposits towards its top (e.g. Larssen et al., 2002). The 2nd megasequence
166 contains Middle Carboniferous-Late Permian clastics in its lower part and carbonates in its upper
167 part, with evaporites present in basinal areas (e.g. Larssen et al., 2002). The very top of the 2nd
168 megasequence is dominated by bioclastic limestones that pass upwards into cherts and siliceous
169 limestones (e.g. Larssen et al., 2002). A subaerial unconformity separates the underlying late
170 Paleozoic carbonates from the overlying Early Triassic-Middle Jurassic strata of the 3rd
171 megasequence (e.g. Glørstad-Clark et al., 2010). This megasequence boundary marks a transition
172 from carbonate-dominated deposition to siliciclastic-dominated sedimentation. The base of the
173 3rd megasequence comprises predominantly fine-grained shelf clastics, whereas the rest of the

174 unit is dominated by shallow marine and coastal clastic rocks (e.g. Glørstad-Clark et al., 2010).
175 This megasequence is unconformably overlain by a succession of Late Jurassic to Early Cretaceous
176 marine mudstones and thin sandstones, which together form the 4th megasequence (e.g.
177 Glørstad-Clark et al., 2010). The uppermost, Late Cretaceous part of the 4th megasequence is
178 generally composed of mudstones with thin intervals of limestones and sandstones (Faleide et
179 al., 1984, 1993, 2008; Gabrielsen, 1984; Gabrielsen et al., 2016). The 5th and 6th megasequences
180 are Cenozoic and consist mainly of marine mudstones with minor siltstones and sandstones
181 (Faleide et al., 1984, 1993, 2008; Gabrielsen, 1984; Gabrielsen et al., 2016).

182 From the description above, it is clear that strong mechanical competency contrasts exist
183 throughout the sedimentary succession in the SW Barents Sea, with relatively weak mudstone-
184 rich intervals alternating with relative strong, carbonate- and sandstone-dominated intervals.
185 This is especially clear between the 3rd and 4th megasequences, where the sandstone-rich upper
186 part of the 3rd megasequence passes upwards into the mudstone-dominated base of the 4th
187 megasequence (Fig. 2). These mechanical competency contrasts are important in terms of the
188 formation and evolution of the normal faults and their associated folds that form the focus of
189 our study.

190

191 Data

192 We used the Fruholmen 3D seismic reflection data, which was acquired and processed by
193 WesternGeco in 2007 and retrieved from the DISKOS database in late 2019

194 (<https://portal.diskos.cgg.com/whereoil-data/>). It is a post-stack time migrated (PSTM) seismic
195 reflection cube that covers an area of c. 533 km². The survey in-lines trend broadly ENE, whereas
196 the cross-lines trend broadly NNW. The studied fault (i.e., the TFFC) changes strike within the
197 study area (see below), so we use arbitrary seismic lines, locally oriented normal to strike, to
198 conduct our quantitative analysis of fault structure and throw (see below). The total record
199 length of this survey reaches 5.5 seconds two-way time (TWT). The data were acquired with a
200 group interval of 12.5 meters (m), a shot point interval of 18.75 m, and a streamer length of 5000
201 m. The original sampling interval for this data was 2 milliseconds (ms), which was resampled
202 during data processing (by WesternGeco) to 4 ms. The data was time migrated using Kirchhoff
203 migration, and an amplitude gain was applied at the last stage of the data processing sequence.
204 A full processing report can be accessed from the DISKOS database
205 (<https://portal.diskos.cgg.com/whereoil-data/>) by searching for “Fruholmen 3D”. The data have
206 a dominant frequency of 40 Hz (see Fig. 1 in supplementary material for complete frequency
207 spectrum) and a vertical resolution (over the depth range of interest; c. 1000 m – 3500 m) of c.
208 12.5 – 25 m, based on an average velocity of 2000 m/s – 4000 m/s, values which are derived from
209 sonic log data. This depth interval covers the syn-kinematic stratigraphy and fault-related folds
210 studied here.

211 In addition to the 3D seismic reflection data, one wellbore (7124/4-1 S) is available in the study
212 area. The wellbore has basic lithostratigraphic data that was retrieved from the Norwegian
213 Petroleum Directorate (<https://factpages.npd.no/en/wellbore/pageview/exploration/all/6678#>)
214 However, no checkshot surveys were available from the well to tie it to the seismic reflection
215 data. Sonic log data (DT) were available for depths of c. 500 m to the well total depth (2730 m),

216 but other logs, like the density log (RHOB), were only available for depths from c. 1200 m to c.
217 2700 m. We therefore used a modified seismic-well tie workflow to generate a reliable TDR and
218 to establish an age-constrained seismic-stratigraphic framework for our specific study area (see
219 supplementary materials for a detailed description of our seismic-well tie workflow).

220

221 Methods

222 Seismic interpretation

223 Our seismic interpretation comprised two main stages. The first stage represented an initial
224 regional interpretation to define the overall basin structure and context of the TFFC. The second,
225 more detailed stage of interpretation focused on the TFFC in the southwest part of the study
226 area. During the regional interpretation, we mapped seven key horizons that represented
227 surfaces that mark major changes in seismic facies; these surfaces represent the top of the
228 acoustic basement (Caledonian), top Permian-Carboniferous, top Lower Triassic, top Upper
229 Triassic, top Jurassic, top Cretaceous, and base Quaternary (Fig. 2). Our detailed interpretation
230 was performed on a cropped seismic volume around the TFFC and included 25 additional
231 horizons that represent two intra-Paleogene, 10 intra-Cretaceous, five intra-Jurassic, and eight
232 intra-Triassic surfaces. These interpreted horizons were used in the geometric and kinematic
233 analysis of the fault, in particular the construction of strike-projections (Walsh and Watterson,
234 1991) and the timing of key periods of fault and fold growth. Given the poor seismic resolution
235 at depth and the lack of well penetrations, it is difficult to distinguish between the 1st and 2nd

236 megasequences, meaning they were combined into one seismic package (Permian –
237 Carboniferous; Fig. 2).

238 We also used seismic attributes and colour blending techniques to help highlight and map fault
239 networks. First, we used a variance seismic attribute that highlights discontinuities in the seismic
240 signal by returning low values for continuous events and high values for discontinuous events
241 (Randen et al., 2001). Second, we colour-blended dip, tensor, and semblance attributes to create
242 a volume that images faults as relatively dark features (for detailed description and definition of
243 these seismic attributes, please refer to Iacopini et al. (2016) and references therein). Guided by
244 the seismic attributes and colour blended volume, we mapped the fault segments in the seismic
245 reflection volume using composite lines taken perpendicular to the strike of the fault segments
246 as seen on the attribute slices. We mapped the fault segments on lines that were spaced every
247 150 m.

248

249 [Fault kinematic analysis](#)

250 Our kinematic analysis of the TFFC involved the analysis of the distribution and style of strain
251 along and between its constituent segments (e.g. Peacock & Sanderson, 1991; Childs et al., 1995;
252 Childs et al., 2019). In this study, we drew on the methods summarised in Jackson et al. (2017).
253 The first step was to study the temporal and spatial evolution of the fault segments using time-
254 structure and time-thickness (isochron) maps. Isochron maps record changes in subsidence and
255 accommodation related to fault and fold growth (e.g. Gawthorpe et al., 2003; Morley, 2002;

256 Schlische, 1995; Young et al., 2001; Jackson & Rotevatn, 2013). Isochron map analysis also helps
257 highlight temporal and spatial trends in across-fault thickening, which helps determine fault
258 growth style (e.g. Jackson et al., 2017). Next, we performed throw analysis by creating throw-
259 length (T-x) profiles (e.g. Baudon & Cartwright, 2008; Cartwright et al., 1995; Dawers & Anders,
260 1995; Gupta & Scholz, 2000; Mansfield & Cartwright, 1996; Rykkelid & Fossen, 2002; Jackson &
261 Rotevatn, 2013; Jackson et al., 2017). We collected throw values on composite seismic lines
262 oriented perpendicular to fault strike every c. 150 m. We could then visualise how throw varies
263 across the fault surface ('strike-projections'; Walsh and Watterson, 1991; see also Duffy et al.,
264 2015). The strike-projections were used to further understand the geometric and kinematic
265 evolution of faults and adjacent folds (e.g. Jackson & Rotevatn, 2013; Jackson et al., 2017;
266 Collanega et al., 2019; Deng & McClay, 2021).

267 In our study, we measured two types of throw values at each (150 m-spaced) position along the
268 fault (Fig. 3). These were labelled *observed throw* and *projected throw* to denote the difference
269 between values that did or did not include so-called *continuous deformation* (i.e. folding),
270 respectively (Walsh & Watterson, 1991; Walsh et al., 1996; Fig. 3). We could then calculate and
271 display the difference between observed and projected throws to give a measure of the extent
272 and magnitude of folding across the fault surface, given the difference between these values is
273 essentially a proxy for fold amplitude. Throw data collected using so-called *projected horizons*
274 mitigated the local effects of fault scarp erosion, which mainly impacted the post-Triassic
275 succession (Fig. 3b).

276

277 Results

278 Structural framework

279 There are three major normal fault systems in the study area (Fig. 4a, b). The first one is a
280 basement-rooted normal fault system (the TFFC; Fig. 4c). The TFFC strikes NW-SE and dips ENE.
281 However, in the NW corner of the study area, the TFFC strikes E-W and dips N. In detail, the TFFC
282 exhibits significant lateral variation of plane geometry with some pronounced strike bends (Fig.
283 4a.iii). The fault plane exhibits a planar geometry in some areas (Fig. 5a, b, e, f), while in others
284 the fault plane shows more of a 'ramp-flat-ramp' fault geometry (Fig. 5c, d) (e.g. Rotevatn &
285 Jackson, 2014). Based on its relatively large throw (locally >2 km; see below) and the seismic
286 facies of the deepest, seismically imaged material it displaces, the TFFC is likely rooted in
287 crystalline basement (i.e., Caledonian) rocks. This observation is also confirmed by previous
288 studies using seismic reflection, gravity, and magnetic data (e.g. Gabrielsen, 1984; Faleide et al.,
289 2008; and Indrevær et al., 2013). The upper tip of the TFFC is typically located within Cretaceous
290 rocks (Figs. 4c and 5). The maximum throw on the TFFC is c. 670 ms (c. 1120 m) (across horizon
291 T5) and c. 1045 ms (c. 1742 m) (across horizon J4) for observed and projected throws, respectively
292 (Fig. 5). Maximum throw values for horizons T5 and J4 are observed at the same location, towards
293 the NW end of the TFFC. When examined closely using seismic attribute time slices, the TFFC
294 appears to be comprised of four distinct geometrical segments (Fig. 4a). These segments are 6-
295 12 km long and have maximum throws that range from c. 339-669 ms (c. 565-1115 m) and c. 634-
296 1044 ms (c. 1057-1740 m) for observed (across horizon T5) and projected (across horizon J4)
297 throws, respectively. The TFFC generally lacks any clear abandoned hanging wall or footwall

298 splays, which suggests that relay ramps did not develop between these segments (Fig. 4ai, ii).
299 Instead, the TFFC is associated with clear along-strike bends (Fig. 4a). The location of these bends
300 corresponds with the approximate tips of the segments comprising the larger TFFC (Fig. 4aiii).
301 Fault-normal anticlines also define paleo-segment boundaries, with synclines developed at the
302 centres of the four flanking segments (Fig. 4a.iii, b.iii).

303 The second fault system exists in the hanging wall of the TFFC and consists of curvilinear, ENE-
304 WSW striking faults that in some cases are >40 km long (Fig. 4a.iii). These faults tend to dip N
305 and die-out to the WSW before linking with the TFFC (Fig. 4a, b). The bottom tip lines of these
306 faults are typically located in the base of the Lower Triassic succession, whereas the upper tip
307 lines are in uppermost Jurassic-lowermost Cretaceous strata (Fig. 4c). Compared to the TFFC,
308 these E-W striking faults have relatively low throws (c. 40 – 60 ms). The ENE-WSE-striking fault
309 system terminates against or just before the folds located in the hanging wall of the TFFC (Fig.
310 4b.ii, iii) suggesting the former are not responsible for the formation of the latter.

311 The third fault system is present in the northern part of the study area and consists of numerous
312 relatively short faults (c. 10 – 30 km) that strike NE-SW and dip N-NW (Fig. 4a, b). Like the second
313 fault system, these faults have their upper tips located in the Upper Jurassic-Lower Cretaceous
314 strata; however, their basal tips are typically located at deeper depths (i.e., in Upper Permian
315 strata; Fig. 4c). The faults in this system tend to have modest throws (up to 200 ms).

316

317 Fault-related folding

318 Fault-parallel folding

319 Strike-perpendicular seismic sections show extensive deformation of hanging wall strata
320 immediately adjacent to the TFFC (Fig. 5). The main structure is a fault-parallel hanging wall
321 syncline that is best-developed in Triassic and Jurassic strata (Fig. 5a). Underlying Paleozoic
322 stratigraphy and overlying Cretaceous stratigraphy are not or are only very gently folded, i.e.
323 Palaeozoic strata are simply offset across the TFFC, whereas Lower Cretaceous strata onlaps onto
324 underlying, folded Jurassic unit (Fig. 5). Along the NW portion of the hanging wall of the TFFC,
325 antithetic and synthetic faults occur, in particular within the gently folded Triassic interval (Fig.
326 5c, d, f).

327

328 Fault-perpendicular folding

329 We also observe significant fault-perpendicular folding along the TFFC, with major hanging wall
330 synclines and anticlines forming along strike of the fault system, especially along its south-
331 eastern portion (Fig. 6). These large, broad folds are up to 5 km wide and have a maximum
332 amplitude of c. 180 ms (c. 300 m) (Fig. 6). A composite seismic line running parallel to the TFFC
333 shows that the pre-Jurassic succession is tabular, albeit folded. In contrast, the overlying
334 Jurassic interval thins across the anticlines and thickens into the flanking synclines (Fig. 6).
335 However, we cannot clearly see similar thickness changes in the Jurassic sequence on seismic
336 lines trending perpendicular to the fault, a key observation that we return to below (Fig. 5a, b).

337 Towards the NW part of the TFFC, folding is less apparent (Fig. 6). This decrease in folding
338 spatially coincides with an area where the TFFC is physically linked to the NE-SW-striking fault
339 system (i.e. the third fault system described above; see also Fig. 4a).

340

341 Spatial distribution of folding

342 We can visualise the distribution of folding across and along the fault surface in two ways. The
343 first and simplest way is by looking at folding at specific structural levels (Fig. 7). The second way
344 is by using strike-projections to display how folding varies across the entire fault surface, i.e.,
345 areas of enhanced folding are marked by large differences between the observed and projected
346 throw on the strike-projection (Fig. 8). The latter method reveals that the folding along the TFFC
347 seems to be restricted to the sedimentary cover next to the fault, being most prominent in Upper
348 Triassic to Upper Cretaceous strata (Fig. 8c). In detail, there are three distinct areas or patches of
349 folding, which are all greatest at the structural level of the Jurassic (Fig. 8c). The sedimentary
350 sequence that appears to be most folded corresponds to a highly stratified interval where
351 differences in rheology and mechanical properties may be expected to be the highest (i.e.
352 megasequences 3-4; Figs. 2 and 8c). Less prominent folding is also observed in the deeper Lower
353 Triassic to Permian-Carboniferous intervals, typically near the centres of the segments
354 comprising the TFFC (Fig. 8c); this is clearly seen in the throw-length plot for the Lower Permian
355 horizon, where the projected and observed throw lines are almost equal along the length of the
356 structure (Fig. 7d).

357 The intensity of folding in the Lower Triassic to Lower Jurassic interval appears to increase
358 towards the NW, with the maximum observed throw difference of c. 300 ms (c. 500 m) being
359 observed near the centre of fault segment D (Figs. 7b, c and 8c). Whereas both discontinuous
360 (i.e. faulting) and continuous (i.e., folding) strain appear to generally increase towards the NW
361 (Fig. 8a, b), on the *projected* throw strike-projection we note four clear throw maxima that are
362 spatially linked to and define the centres of the constituent segments of the TFFC (Fig. 8a). In
363 contrast, the *observed* throw strike-projection surface shows only two clear throw maxima that
364 spatially correlate to the centres of segments B and D, and a less prominent throw maximum
365 towards the SE that corresponds to the centre of segment A (Fig. 8b). This is supported by the
366 throw-length plots in Fig. 7, which show that significant changes in throw or fold magnitude
367 correlate with fault branchlines. More specifically, we notice an abrupt decrease in throw
368 magnitude in areas where strain is partitioned between the main fault and intersecting faults
369 (Fig. 8).

370 The northwesternmost segment of the TFFC (segment D) has notably higher throw than
371 segments to the SE (up to c. 670 ms (c. 1120 m) and c. 1100 ms (c. 1835 m) for observed and
372 projected throws, respectively, compared to c. 500 ms (c. 835 m) and 700 ms (c. 1170 m) for the
373 other segments; Figs. 5f; 7b-d and 8). A potential explanation for the difference in throw between
374 segment D and other segments is that the throw on the former reflects combined slip on at least
375 two faults; the TFFC itself, plus a series of intersecting fault segments likely related to the NE-SW
376 fault system imaged on the fault attribute slices in Fig. 4a.i, ii. The impact of splay faulting on
377 these locally high throws becomes clearer when we examine the hanging wall and footwall cut-
378 off points on the strike-projection surfaces (Fig. 8) and the throw-length plots (Fig. 7b-d); on these

379 we can see an increase in the magnitude of folding and fault displacement at fault branchlines.
380 The fact that the NW ends of the TFFC are not imaged within the study area makes it difficult to
381 determine the geometric link between segment D and adjacent structures.

382

383 [Origin of fault-related folding](#)

384 Different processes can account for the folding, and specifically fault-parallel folding, next to the
385 TFFC. First, the folding could be a result of horizontal compression related to basin inversion.
386 However, this is not the most likely scenario, given the lack of regional evidence for an Early
387 Cretaceous compressional event, and the fact that the observed fold geometries and onlap
388 relationships are not consistent with inversion, e.g., the syn-kinematic strata we observe here is
389 not folded, and onlaps onto the fault-perpendicular anticlines and onto the steep, basinward
390 dipping limbs of the fault-parallel syncline, whereas syn-inversion growth strata typically onlaps
391 onto the inversion fold, with the earliest or oldest growth strata being folded (e.g. Coleman et
392 al., 2019). Another possible causal mechanism is frictional drag folding (e.g. Schlische, 1995).
393 However, the folds formed along the TFFC are wide (>100s meters), and this is not likely to be
394 the result of drag folding, which typically forms far narrower folds (10s – 100s meters) (Coleman
395 et al., 2019) (Figs. 5a, f and 9a, b). We therefore interpret that the fault-parallel folds are fault-
396 propagation folds, formed ahead of the propagating (upper and lower) tips of normal faults (e.g.
397 Withjack et al., 1990; Allmendinger, 1998; Cosgrove & Ameen, 1999; Hardy & McClay, 1999;
398 Gawthorpe & Leeder, 2000; Withjack & Callaway, 2000; Coleman et al., 2019; Jackson et al.,
399 2020). In fact, vertical fault propagation can also produce frictional drag folds, which might be

400 synthetic dip panels (i.e. layers dipping in the same direction) that are remnants of fault tip
401 folding (see Ferrill et al., 2012, 2017 for more details).

402 Changes in fault plane geometry might also be responsible for the formation of small-scale fault-
403 perpendicular and fault-parallel folds (Ehrlich & Gabrielsen, 2004). For instance, areas where the
404 fault plane is curved (convex or concave) seems to coincide with some of the folding we noted in
405 the Jurassic and Triassic intervals (Fig. 5c-e and 6c). These folds can potentially superimpose
406 smaller structures onto larger ones, or simply augment and amplify the larger structures.
407 However, we interpret that the fault-perpendicular folds (Fig. 6) represent now-breached
408 segment boundaries between the lateral tips of precursor faults given their prevalence near the
409 mapped lateral tips (i.e. displacement minima) of TFFC fault segments (e.g. Gawthorpe et al.,
410 1997; Corfield & Sharp, 2000; Sharp et al., 2000; Willsey et al., 2002; White & Crider, 2006; Kane
411 et al., 2010; Duffy et al., 2013; Khalil & McClay, 2017; Tavani et al., 2018; Coleman et al., 2019).
412 These changes in fault plane geometry might have led to the formation of different fold styles
413 along-strike of the TFFC. For example, where the fault plane is planar (Fig. 5a, b, e, f), we tend to
414 observe a relatively simple, monocline-style of folding in the hanging wall of the TFFC (Fig. 9a, b,
415 e, f). In contrast, in areas where the fault plane shows more of a 'ramp-flat-ramp' fault geometry
416 (e.g. Rotevatn & Jackson, 2014), an anticline-syncline pair is present (Figs. 5c, d and 9c, d). The
417 former folding style (i.e. fault-parallel monocline) is consistent with our earlier interpretation of
418 extensional folding due to upward propagation of the fault tip (e.g. Khalil and McClay, 2002;
419 Ferrill et al., 2007; Conneally et al., 2017; Smart and Ferrill, 2018). Although differential
420 compaction can also form monoclines above planar faults (e.g. Fig. 5 in Skuce, 1996), it would
421 not result in the syn-kinematic strata onlapping onto the monocline's basinward-facing steep

422 limb like we observe here (Fig. 9a, b, e, f). This onlap relationship indicates the fold grew whilst
423 at-surface rather than after some burial as required by a differential compaction model. For the
424 latter style of folding (i.e. anticline-syncline pairs) we note a correlation between the location of
425 these anticline-syncline pairs and changes in fault plane geometry, and we interpret the origin of
426 these folds as a result of changes in fault (e.g. Gibbs, 1984; McClay & Scott, 1991; Rotevatn &
427 Jackson, 2014; [Deng and McClay, 2019](#); [McHarg et al., 2020](#)).

428

429 [Temporal evolution of the TFFC](#)

430 Having established the present structural style of the TFFC and described its geometry, we now
431 focus on how this fault system developed through time. We do this by studying thickness
432 variations in syn-kinematic stratal units along and across fault arrays (e.g. Cowie et al., 2000;
433 McLeod et al., 2000; Gawthorpe et al., 2003), as well as the spatial distribution of the fault-
434 propagation folds described in the previous section; together these observations help us
435 determine the position of now-breached segment boundaries and the style of propagation
436 (surface breaching vs. buried) of the TFFC (e.g. Gawthorpe et al., 1997; Corfield & Sharp, 2000;
437 Sharp et al., 2000). For each interpreted stratigraphic unit, we present our observations first and
438 then provide possible interpretations that could explain how the TFFC evolved during that time
439 period.

440 Carboniferous – Permian (350-250 Ma)

441 The first seismic package above the crystalline basement is assigned a Carboniferous to Permian
442 age, which makes it lithostratigraphically equivalent to the 1st and 2nd megasequences (Fig. 2).
443 No clear thickness variations are observed across the TFFC during this period (Fig. 10a). However,
444 these Paleozoic strata seems to thicken regionally towards the NE, away from the TFFC, as well
445 as thickening (by c. 70 ms or c. 150 m) across relatively small faults in its footwall (Fig. 10a).

446 The lack of thickness variations across the TFFC suggests that the fault was not active at this time,
447 although smaller, E-W striking faults in its footwall may have been (Fig. 10a). This style of strain
448 partitioning may have arisen because the smaller faults were more optimally oriented to
449 accommodate N-S-directed stretching associated with this initial period of relatively mild
450 extension (Rift Phase 2; Fig. 2). Regional NE thickening of this seismic package might be related
451 to the long wavelength variations in basin subsidence related to regional tectonic events.

452 Early Triassic (251-245 Ma)

453 The second stratal unit is Early Triassic and represents the Klappmyss Formation (Fig. 2). This
454 mudstone-dominated unit is generally well-imaged in seismic data and shows no significant
455 thickness variations across the TFFC, or across the entire area of interest (Fig. 10b). The only
456 exception to this is the clear across-fault thickening seen in association with the N-dipping fault
457 segment defining the NW portion of the TFFC (e.g. segment D; Figs. 5f and 10b). These thickness
458 variations (up to 200 ms, c. 360 m thick) suggest that this segment was active during this period,
459 while others were inactive.

460 Middle Triassic (245-227 Ma)

461 The third stratal unit is Middle Triassic and represents the Kobbe and Snadd formations (Figs. 2
462 and 5c). This unit displays significant thickness variations (43 to 346 ms, c. 80 to 620 m) across all
463 segments of the TFFC, and more minor variations along a NE-SW-striking fault segment located
464 in the NE part of the study area (Figs. 5c and 10c). These thickness variations suggest that
465 segments A-D of the TFFC, along with a NE-trending fault in its hanging wall, were all active during
466 this period.

467 Late Triassic (227-201 Ma)

468 The fourth stratal unit is Late Triassic and represents the Fruholmen Formation (Figs. 2 and 5c).
469 This unit shows thickening across the NE- trending fault segment (segment D), and minor
470 thickness variations across segments A-C of the TFFC (Fig. 10d). In fact, the strata appear to thin
471 towards the TFFC, suggesting that the fault was likely buried and expressed by a fault-
472 propagation fold during this period (Fig. 10d).

473 Jurassic (200-150 Ma)

474 The fifth stratal unit is Jurassic and mostly includes the upper part of the 3rd megasequences (Fig.
475 2). This unit includes all the Jurassic formations and is well-imaged in seismic data, except for
476 areas immediately next to the TFFC where bedding is relatively steep and rocks may be highly
477 faulted (Fig. 5c, f). Despite being relatively thin, this unit shows significant thickness variations
478 across and along the TFFC (Fig. 10e). More specifically, we see significant synclinal depocenters
479 (up to 170 ms, c. 302 m thick) near the centres of all fault segments, with Jurassic strata thinning

480 across and onlapping onto fault-perpendicular anticlines *and* onto the relatively steep,
481 basinward-dipping limbs of the fault-parallel syncline (Figs. 9d and 10e). However, the Jurassic
482 stratal unit, having thinned onto the steep dipping limb, then thickens towards the surface of the
483 TFFC (Fig. 9d). The overall across-fault thickening also differs *along strike* of the TFFC, with the
484 maximum across-fault thickening (130 ms or c. 230 m) occurring along segment D (Fig. 10e).

485 The observed onlap relationships and thickness variations across and along-strike of the TFFC
486 suggest that many of the fault-propagation folds described above formed during the Early
487 Jurassic (start of Rift Phase 3; Fig. 2). However, this stage of fault-propagation folding might have
488 been restricted to segments B-D of the TFFC. Therefore, we tentatively suggest that segments B-
489 D rapidly formed and linked laterally during the Late Triassic to Early Jurassic, before linking to
490 segment A. The fact that the fault-propagation folding was the prominent at-surface
491 deformation style in the Jurassic, when earlier, during the Triassic, the fault was a surface-
492 breaching structure, requires that the fault was reburied between the Late Triassic to Early
493 Jurassic. Having breached the surface, it is clear from thinning of the footwall strata and the
494 presence of hanging wall depocenters that by the end of the Jurassic, the TFFC was a single,
495 through-going fault system (Fig. 10e).

496 Cretaceous (132.6-97.5 Ma)

497 The youngest stratal unit is Cretaceous and is lithostratigraphically equivalent to the 4th
498 megasequence (Fig. 2). This relatively thick unit (up to 870 ms, c. 1240 m) displays an overall
499 wedge-shaped geometry on seismic data, a geometry that is classically associated with syn-
500 kinematic strata (e.g. Fig. 5a) (Prosser, 1993). However, we further subdivide the unit into three

501 sub-units based on intraformational onlap relationships (Fig. 5). The lowermost sub-unit onlaps
502 onto and thins towards the underlying Jurassic unit forming the steep, basinward dipping limb
503 of the TFFC hanging wall syncline. This sub-unit is absent in the immediate hanging wall of the
504 fault and from the fault footwall (Figs. 5 and 9). These geometries suggest that the TFFC was
505 acting as a blind, fully linked fault at this stage, leading to fault-propagation folding of cover strata
506 and the formation of an at-surface, basinward-facing monocline (e.g. Sharp et al., 2000) (Figs. 6
507 and 10f). Thus, having broken surface again during the Jurassic, the fault was reburied, such that
508 during the Early Cretaceous the fault was expressed at the surface as a fault-propagation fold. In
509 the north of the study area, in contrast to that seen along the main part of the TFFC, the lower
510 sub-unit thickens across the NE-SW-striking segment in the hanging wall of the larger structure
511 (Fig. 10f). Thickening of this sub-unit along the entire strike length of this fault suggests that this
512 was actively accruing displacement as a single, continuous, relatively long structure (c. 35 km)
513 (Fig. 10f).

514 The middle Cretaceous sub-unit, in comparison to the lowermost one, thickens (rather than
515 thins) towards the NE-dipping segments of the TFFC, defining several clear, fault-bound
516 depocenters (i.e., A-C). This unit is partially absent in the footwalls of these segments (Fig. 10g).
517 At its base, this sub-unit locally onlaps the underlying, basinward-dipping, lowermost sub-unit;
518 this onlap is not, however, as pronounced as that observed at the base of the lowermost sub-
519 unit, which onlaps onto basinward-tilted Jurassic strata (Figs. 5a-c and 9a-c).

520 The distribution of the uppermost Cretaceous sub-unit defines several large, fault-bound
521 depocenters, with basal and intraformational onlap towards the TFFC being absent (Figs. 9 and

522 10h). There is also a notable across-fault thickening along a NE-SW-striking segment that is likely
523 part of the ENE-WSW fault system, as opposed to the TFFC (Figs. 4a and 10h).

524 The presence of discrete fault- rather than fold-bound depocenters in the middle and upper parts
525 of the Cretaceous, as defined by the distribution and seismic-stratigraphic architecture of the
526 related sub-units, suggest that, by this time, the TFFC had breached its overlying fault-
527 propagation fold to form a classic, half-graben-style depocenter. We interpret that this
528 depocenter was segmented along-strike due to the along-strike variations in accommodation
529 created by differential compaction of underlying strata across earlier-formed (i.e., Triassic and
530 Jurassic) fault-propagation folds . This is supported by the lack of any clear fault-perpendicular,
531 syncline-anticline pairs along-strike of the TFFC (Fig. 6) and the overall decrease in throw
532 magnitude at the Cretaceous structural level (Figs. 7a and 8).

533 Summary

534 In summary, we suggest that the TFFC initiated during the Early – Middle Triassic, with fault
535 segments B, C and D rapidly forming and linking laterally during the Middle Triassic(Fig. 10).
536 During this period (Middle Triassic), the TFFC was a surface-breaching structure. However, the
537 TFFC was subsequently reburied between the Late Triassic and Early Jurassic, with continued
538 upward propagation of the fault forming a fault-propagation fold at the free surface. By the Late
539 Jurassic the TFFC broke the surface again and was a single, through-going fault system. The fault
540 was subsequently reburied again, such that during the Early Cretaceous it was expressed at the
541 surface as a fault-propagation fold. The TFFC again breached its overlying fault-propagation fold
542 to form a classic, half-graben-style depocenter at the time of deposition of the middle and

543 uppermost Cretaceous stratal units. Therefore, the TFFC has experienced two distinct phases of
544 fault-propagation folding during its lifetime.

545

546 Discussion

547 Current models show that extensional fault-propagation folds are formed during the early stages
548 of extension, with initially intact monoclines subsequently being breached by their causal faults
549 (e.g. Gawthorpe & Leeder, 2000; Sharp et al., 2000; Jackson & Lewis, 2016; Coleman et al., 2019;
550 Deng & McClay, 2019). Our work on the TFFC shows that the start of fault-propagation folding is
551 marked by the thinning and onlap of the Lower Jurassic strata towards the fault onto the NE-
552 dipping limb of the Upper Triassic hanging wall syncline (Figs. 5 and 9). However, a second phase
553 of fault-propagation folding likely occurred during the Early Cretaceous as marked by the onlap
554 of growth strata onto the underlying Jurassic unit, and the overall thinning of the Lower
555 Cretaceous towards the TFFC (Figs. 9 and 10f). The thickening of overlying Cretaceous units
556 towards the fault indicates that the fault had breached the fault-propagating fold at this time
557 (Fig. 10g, h). Therefore, the fault-propagation folds we observe did not simply form during the
558 earlier phase of extension, but seemingly are best-developed during the Jurassic and, especially,
559 the Cretaceous, after the fault had been active for some time. Based on our borehole-constrained
560 seismic-stratigraphic framework, we show that fault-propagation folds can form over periods of
561 c. 25.7 Myr (1st phase of folding) and c. 32 Myr (2nd phase of folding). Multiple phases of
562 superimposed fault-propagation folding can therefore occur if a fault is subsequently reburied
563 during times of: (i) relatively low tip propagation rates (relative to a constant, long-term,

564 sediment accumulation rate); and/or (ii) relatively high sediment accumulation rate (relative to
565 a constant, long term, tip propagation rate).

566 Previous studies have shown that changes in fault dip direction and the presence of multiphase
567 extension results in complex hanging wall fold and fault geometries (Coleman et al., 2019; Deng
568 & McClay, 2019). Our results from the TFFC show that despite the presence of multiphase
569 extension and associated changes in fault geometry as a function of growth patterns, the
570 geometry of the studied fault-propagation folds remained relatively simple. This is probably
571 because the area experienced coaxial rifting and did not undergo dramatic changes in extension
572 direction. However, our study confirms the complicated nature of syn-kinematic hanging wall
573 strata and fault geometries as a result of folding before the fault reaches the surface and forms
574 a scarp. The fault propagation folding and secondary structures observed in the area have led to
575 the formation of complex syn-kinematic hanging wall geometries, with stratal units thinning onto
576 the fold limb and other units thickening towards the fault. These different observed geometries
577 suggest that the nature of syn-kinematic hanging wall strata can be more complex than the classic
578 wedge-shaped cross-sectional geometry often described from extensional basins (e.g. Prosser,
579 1993).

580 Differences in host rock rheology, fault propagation rate, and throw magnitude can lead to spatial
581 variability in the size and distribution of fault-propagation folds (Mansfield & Cartwright, 2000;
582 Coleman et al., 2019). The fault-propagation folds we studied appear to have preferentially
583 developed above the upper tip line of the TFFC within mechanically weak/incompetent layers
584 (Fig. 8c). As discussed above, the constituent segments of the TFFC fault segments likely linked

585 relatively rapidly during the Late Triassic – Early Jurassic (Figs. 7c and 10d, e). Rapid linkage, which
586 may have been associated with high displacement rates, might account for relatively poor
587 development of fault-propagation folds at the Jurassic structural level (Figs. 5d, f and 6). In
588 contrast, the well-developed Early Cretaceous fault-propagation folds probably reflect a period
589 of relatively low displacement rates on the TFFC. This period of low displacement rates during
590 the Early Cretaceous is consistent with our regional understanding of rift phases as it correlates
591 with very end of Rift Phase 3 (Fig. 2). Additionally, the Lower Cretaceous interval is dominated by
592 mudstone, which we infer is relatively weak and deforms in a more ductile manner, whereas the
593 underlying Jurassic section is more heterogenous, comprising relatively strong and brittle
594 sandstone and siltstone layers at its base, and weaker and more ductile mudstone near its top.
595 We therefore infer that well-developed fault-propagation folds formed in the weaker and more
596 ductile Early Cretaceous mudstones and a relatively poorly-developed fault-propagation folds in
597 the more the mechanically layered stratigraphic Jurassic sequence (e.g. Conneally et al., 2017;
598 Lăpădat et al., 2017; Roche et al., 2020). Despite differences in how well-developed the fault-
599 propagation folds are at the various structural levels, they appear to be confined to the upper,
600 relatively mechanically weak or incompetent units (i.e. megasequences 3-5) capping the more
601 competent, deeper units (i.e. megasequences 1-2). Similar cases of folding being restricted to
602 upper units with lower deeper units acting as forcing members are described in literature (e.g.
603 Maurin & Niviere, 1999; Sharp et al., 2000; Jackson et al., 2006).

604 Even though the importance of considering ductile deformation when assessing normal fault
605 growth has long been recognized (e.g. Walsh & Watterson, 1991), this notion has only relatively
606 recently seen a broader support due to the increasing use of high-quality 3D seismic reflection

607 data, and the study of exceptional field exposures that reveal the complex three-dimensional
608 geometry of normal faults and related folds (e.g. Childs et al., 2002; Walsh et al., 1999, 2002,
609 2003; van der Zee & Urai, 2005; Schöpfer et al., 2006; Long & Imber, 2010; Giba et al., 2012;
610 Jackson & Rotevatn, 2013; Duffy et al., 2015; Fossen & Rotevatn, 2016; Conneally et al., 2017;
611 Freitag et al., 2017; Camanni et al., 2019; Jackson et al., 2020; Roche et al., 2020, 2021; Deng &
612 McClay, 2021). Our study further highlights the value of considering both discontinuous (i.e.,
613 faulting) and continuous (i.e., folding) deformation when studying normal fault growth. We show
614 that a significant proportion of strain (10 – 40%; see Fig. 4 in supplementary material for complete
615 data distribution) along the TFFC is expressed in a ductile manner as (fault-propagation) folding,
616 as opposed to a brittle shear fracturing or faulting. Therefore, not including the continuous
617 component of the strain field will most likely result in erroneous structural restorations or an
618 incomplete understanding of normal fault growth. Our work on the TFFC also suggests that the
619 construction of strike-projections including both discontinuous and continuous strain, and
620 plotting the difference between the two, can be a quick and powerful tool to illustrate the three-
621 dimensional variability of fault-related folds across normal fault surfaces. When integrated with
622 isochron analysis, this can help us determine the patterns and products of normal fault growth,
623 and the origin and evolution of fault-related folds, both of which have major implications for rift
624 morphology and stratigraphic development.

625

626 Conclusions

627 We used high-quality 3D seismic reflection data from SW Barents Sea, offshore Norway to
628 analyse the along-strike variations and geometric evolution of fault-propagation folds associated
629 with a large, basement-involved fault. We showed that this fault system consists of four, hard-
630 linked segments that are 6-12 km long. Fault-perpendicular anticlines, which are flanked by fault-
631 perpendicular synclines, occur at relict segment boundaries (i.e. displacement-gradient folds),
632 whereas fault-parallel folds (i.e. fault-propagation folds) occur along-strike and down-dip of the
633 flanking fault. Based on the fault-fold relationships and the architecture of the nearby
634 stratigraphic record, we suggest that the fault underwent a phase of relatively rapid lateral
635 linkage in the Late Triassic to Early Jurassic. We also show that fault-propagation folding was
636 protracted (c. 57 Myr), occurring in multiple phases due to periodic burial of the fault by syn- and
637 intra-kinematic strata. Our findings further highlight the value of considering both discrete (i.e.,
638 fault-related) and continuous (i.e., fold-related) strain when assessing the processes of fault
639 growth, and the geometry, tectono-stratigraphic evolution, and resource potential of rift basins.
640 Using strike-projections of fault surface is particularly powerful for highlighting 3D variations in
641 faulting and folding, something that may be missed or unclear when using throw-length and
642 throw-depth plots alone.

643

644

645

646 References

- 647 Allmendinger, R. W. (1998). Inverse and forward numerical modeling of trishear fault-
648 propagation folds. *Tectonics*, 17(4), 640–656.
- 649 Baudon, C., & Cartwright, J. (2008). The kinematics of reactivation of normal faults using high
650 resolution throw mapping. *Journal of Structural Geology*, 30(8), 1072–1084.
651 <https://doi.org/10.1016/j.jsg.2008.04.008>
- 652 Bell, R. E., Jackson, C. A. L., Whipp, P. S., & Clements, B. (2014). Strain migration during
653 multiphase extension: Observations from the northern North Sea. *Tectonics*, 33(10), 1936–
654 1963. <https://doi.org/10.1002/2014TC003551>
- 655 Camanni, G., Roche, V., Childs, C., Manzocchi, T., Walsh, J., Conneally, J., Saqab, M. M., &
656 Delogkos, E. (2019). The three-dimensional geometry of relay zones within segmented
657 normal faults. *Journal of Structural Geology*, 129(December 2018), 103895.
658 <https://doi.org/10.1016/j.jsg.2019.103895>
- 659 Cardozo, N. (2008). Trishear in 3D. Algorithms, implementation, and limitations. *Journal of*
660 *Structural Geology*, 30(3), 327–340. <https://doi.org/10.1016/j.jsg.2007.12.003>
- 661 Cartwright, J. A., Trudgill, B. D., & Mansfield, C. S. (1995). Fault growth by segment linkage: an
662 explanation for scatter in maximum displacement and trace length data from the
663 Canyonlands Grabens of SE Utah. *Journal of Structural Geology*, 17(9), 1319–1326.
664 [https://doi.org/10.1016/0191-8141\(95\)00033-A](https://doi.org/10.1016/0191-8141(95)00033-A)

665 Childs, C., Walsh, J. J., & Watterson, J. (1997). Complexity in fault zone structure and
666 implications for fault seal prediction. *Norwegian Petroleum Society Special Publications*,
667 7(C), 61–72. [https://doi.org/10.1016/S0928-8937\(97\)80007-0](https://doi.org/10.1016/S0928-8937(97)80007-0)

668 Childs, C., Watterson, J., & Walsh, J. J. (1995). Fault overlap zones within developing normal
669 fault systems. *Journal - Geological Society (London)*, 152(3), 535–549.
670 <https://doi.org/10.1144/gsjgs.152.3.0535>

671 Childs, Conrad, Holdsworth, R. E., Jackson, C. A. L., Manzcchi, T., Walsh, J. J., & Yielding, G.
672 (2017). Introduction to the geometry and growth of normal faults. *Geological Society*
673 *Special Publication*, 439(1), 1–9. <https://doi.org/10.1144/SP439.24>

674 Childs, Conrad, Nicol, A., Walsh, J. J., & Watterson, J. (2002). The growth and propagation of
675 synsedimentary faults. *Journal of Structural Geology*, 25(4), 633–648.
676 [https://doi.org/10.1016/S0191-8141\(02\)00054-8](https://doi.org/10.1016/S0191-8141(02)00054-8)

677 Childs, Conrad, Worthington, R. P., Walsh, J. J., & Roche, V. (2019). Conjugate relay zones:
678 geometry of displacement transfer between opposed-dipping normal faults. *Journal of*
679 *Structural Geology*, 118(June 2018), 377–390. <https://doi.org/10.1016/j.jsg.2018.11.007>

680 Coleman, A. J., Duffy, O. B., & Jackson, C. A. L. (2019). Growth folds above propagating normal
681 faults. *Earth-Science Reviews*, 196. <https://doi.org/10.1016/j.earscirev.2019.102885>

682 Collanega, L., Siuda, K., A.-L. Jackson, C., Bell, R. E., Coleman, A. J., Lenhart, A., Magee, C., &
683 Breda, A. (2019). Normal fault growth influenced by basement fabrics: The importance of
684 preferential nucleation from pre-existing structures. *Basin Research*, 31(4), 659–687.

685 <https://doi.org/10.1111/bre.12327>

686 Conneally, J., Childs, C., & Nicol, A. (2017). Monocline formation during growth of segmented
687 faults in the Taranaki Basin, offshore New Zealand. *Tectonophysics*, 721(July), 310–321.

688 <https://doi.org/10.1016/j.tecto.2017.06.036>

689 Corfield, S., & Sharp, I. R. (2000). Structural style and stratigraphic architecture of fault
690 propagation folding in extensional settings: A seismic example from the Smorbukk area,
691 Halten Terrace, Mid-Norway. *Basin Research*, 12(3–4), 329–341.

692 <https://doi.org/10.1111/j.1365-2117.2000.00133.x>

693 Corfield, Stephen, Sharp, I., Häger, K. O., Dreyer, T., & Underhill, J. (2001). An integrated study
694 of the garn and melke formations (middle to upper jurassic) of the smorbukk area, halten
695 terrace, mid-norway. *Norwegian Petroleum Society Special Publications*, 10(C), 199–210.

696 [https://doi.org/10.1016/S0928-8937\(01\)80014-X](https://doi.org/10.1016/S0928-8937(01)80014-X)

697 Cosgrove, J. W., & Ameen, M. S. (1999). A comparison of the geometry, spatial organization and
698 fracture patterns associated with forced folds and buckle folds. Geological Society,
699 London, Special Publications, 169(1), 7 LP – 21.

700 <https://doi.org/10.1144/GSL.SP.2000.169.01.02>

701 Cowie, P. A., Gupta, S., & Dawers, N. H. (2000). Implications of fault array evolution for synrift
702 depocentre development: Insights from a numerical fault growth model. *Basin Research*,
703 12(3–4), 241–261. <https://doi.org/10.1111/j.1365-2117.2000.00126.x>

704 Dawers, N. H., & Anders, M. H. (1995). Displacement-length scaling and fault linkage. *Journal of*

705 Structural Geology, 17(5), 607–614. [https://doi.org/10.1016/0191-8141\(94\)00091-D](https://doi.org/10.1016/0191-8141(94)00091-D)

706 Deng, H., & McClay, K. (2019). Development of extensional fault and fold system: Insights from
707 3D seismic interpretation of the Enderby Terrace, NW Shelf of Australia. *Marine and*
708 *Petroleum Geology*, 104(December 2018), 11–28.
709 <https://doi.org/10.1016/j.marpetgeo.2019.03.003>

710 Deng, H., & McClay, K. (2021). Three-dimensional geometry and growth of a basement-involved
711 fault network developed during multiphase extension, Enderby Terrace, North West Shelf
712 of Australia. *GSA Bulletin*, 1–28. <https://doi.org/10.1130/b35779.1>

713 Doré, A. G. (1995). Barents Sea Geology, Petroleum Resources and Commercial Potential.
714 *Arctic*, 48(3), 207–221. <http://www.jstor.org/stable/40511656>

715 Duffy, O. B., Bell, R. E., Jackson, C. A. L., Gawthorpe, R. L., & Whipp, P. S. (2015). Fault growth
716 and interactions in a multiphase rift fault network: Horda Platform, Norwegian North Sea.
717 *Journal of Structural Geology*, 80, 99–119. <https://doi.org/10.1016/j.jsg.2015.08.015>

718 Duffy, O. B., Gawthorpe, R. L., Docherty, M., & Brocklehurst, S. H. (2013). Mobile evaporite
719 controls on the structural style and evolution of rift basins: Danish Central Graben, North
720 Sea. *Basin Research*, 25(3), 310–330. <https://doi.org/10.1111/bre.12000>

721 Ehrlich, R., & Gabrielsen, R. H. (2004). The complexity of a ramp-flat-ramp fault and its effect on
722 hanging-wall structuring: An example from the Njord oil field, offshore mid-Norway.
723 *Petroleum Geoscience*, 10(4), 305–317. <https://doi.org/10.1144/1354-079303-585>

724 Eldholm, O., & Thiede, J. (1980). Cenozoic continental separation between Europe and
725 Greenland. *Palaeogeography, Palaeoclimatology, Palaeoecology*, 30(C), 243–259.
726 [https://doi.org/10.1016/0031-0182\(80\)90060-7](https://doi.org/10.1016/0031-0182(80)90060-7)

727 Faleide, J. I., Tsikalas, F., Breivik, A. J., Mjelde, R., Ritzmann, O., Engen, Ø., Wilson, J., & Eldholm,
728 O. (2008). Structure and evolution of the continental margin off Norway and the Barents
729 Sea. *Episodes*, 31(1), 82–91. <https://doi.org/10.18814/epiiugs/2008/v31i1/012>

730 Faleide, Jan I., Vågnes, E., & Gudlaugsson, S. T. (1993). Late Mesozoic-Cenozoic evolution of the
731 south-western Barents Sea in a regional rift-shear tectonic setting. *Marine and Petroleum*
732 *Geology*, 10(3), 186–214. [https://doi.org/10.1016/0264-8172\(93\)90104-Z](https://doi.org/10.1016/0264-8172(93)90104-Z)

733 Faleide, Jan Inge, Gudlaugsson, S. T., & Jacquart, G. (1984). Evolution of the western Barents
734 Sea. *Marine and Petroleum Geology*, 1(2), 70–78. [https://doi.org/10.1016/0264-](https://doi.org/10.1016/0264-8172(84)90082-5)
735 [8172\(84\)90082-5](https://doi.org/10.1016/0264-8172(84)90082-5)

736 Ferrill, D. A., Morris, A. P., & McGinnis, R. N. (2012). Extensional fault-propagation folding in
737 mechanically layered rocks: The case against the frictional drag mechanism.
738 *Tectonophysics*, 576–577, 78–85. <https://doi.org/10.1016/j.tecto.2012.05.023>

739 Ferrill, D. A., Morris, A. P., McGinnis, R. N., Smart, K. J., Wigginton, S. S., & Hill, N. J. (2017).
740 Mechanical stratigraphy and normal faulting. *Journal of Structural Geology*, 94, 275–302.
741 <https://doi.org/10.1016/j.jsg.2016.11.010>

742 Ferrill, D. A., Morris, A. P., & Smart, K. J. (2007). Stratigraphic control on extensional fault
743 propagation folding: Big Brushy Canyon monocline, Sierra Del Carmen, Texas. *Geological*

744 *Society Special Publication*, 292, 203–217. <https://doi.org/10.1144/SP292.12>

745 Fossen, H., & Rotevatn, A. (2016). Fault linkage and relay structures in extensional settings-A
746 review. *Earth-Science Reviews*, 154, 14–28.
747 <https://doi.org/10.1016/j.earscirev.2015.11.014>

748 Freitag, U. A., Sanderson, D. J., Lonergan, L., & Bevan, T. G. (2017). Comparison of upwards
749 splaying and upwards merging segmented normal faults. *Journal of Structural Geology*,
750 100, 1–11. <https://doi.org/10.1016/j.jsg.2017.05.005>

751 Gabrielsen, R. H. (1984). Long-lived fault zones and their influence on the tectonic development
752 of the southwestern Barents Sea. *Journal of the Geological Society*, 141(4), 651–662.
753 <https://doi.org/10.1144/gsjgs.141.4.0651>

754 Gabrielsen, Roy H., Sokoutis, D., Willingshofer, E., & Faleide, J. I. (2016). Fault linkage across
755 weak layers during extension: An experimental approach with reference to the Hoop Fault
756 Complex of the SW Barents Sea. *Petroleum Geoscience*, 22(2), 123–135.
757 <https://doi.org/10.1144/petgeo2015-029>

758 Gac, S., Hansford, P. A., & Faleide, J. I. (2018). Basin modelling of the SW Barents Sea. *Marine
759 and Petroleum Geology*, 95(May), 167–187.
760 <https://doi.org/10.1016/j.marpetgeo.2018.04.022>

761 Gawthorpe, R. L., & Leeder, M. R. (2000). Tectono-sedimentary evolution of active extensional
762 basins. *Basin Research*, 12(3–4), 195–218. [https://doi.org/10.1111/j.1365-
763 \[2117.2000.00121.x\]\(https://doi.org/10.1111/j.1365-2117.2000.00121.x\)](https://doi.org/10.1111/j.1365-2117.2000.00121.x)

764 Gawthorpe, Rob L., Jackson, C. A. L., Young, M. J., Sharp, I. R., Moustafa, A. R., & Leppard, C. W.
765 (2003). Normal fault growth, displacement localisation and the evolution of normal fault
766 populations: The Hammam Faraun fault block, Suez rift, Egypt. *Journal of Structural*
767 *Geology*, 25(6), 883–895. [https://doi.org/10.1016/S0191-8141\(02\)00088-3](https://doi.org/10.1016/S0191-8141(02)00088-3)

768 Gawthorpe, Rob L., Sharp, I., Underhill, J. R., & Gupta, S. (1997). Linked sequence stratigraphic
769 and structural evolution of propagating normal faults. *Geology*, 25(9), 795–798.
770 [https://doi.org/10.1130/0091-7613\(1997\)025<0795:LSSASE>2.3.CO;2](https://doi.org/10.1130/0091-7613(1997)025<0795:LSSASE>2.3.CO;2)

771 Giba, M., Walsh, J. J., & Nicol, A. (2012). Segmentation and growth of an obliquely reactivated
772 normal fault. *Journal of Structural Geology*, 39, 253–267.
773 <https://doi.org/10.1016/j.jsg.2012.01.004>

774 Gibbs, A. D. (1984). Structural evolution of extensional basin margins. *Journal of the Geological*
775 *Society*, 141(4), 609 LP – 620. <https://doi.org/10.1144/gsjgs.141.4.0609>

776 Glørstad-Clark, E., Faleide, J. I., Lundschieen, B. A., & Nystuen, J. P. (2010). Triassic seismic
777 sequence stratigraphy and paleogeography of the western Barents Sea area. *Marine and*
778 *Petroleum Geology*, 27(7), 1448–1475. <https://doi.org/10.1016/j.marpetgeo.2010.02.008>

779 Gupta, A., & Scholz, C. H. (2000). A model of normal fault interaction based on observations and
780 theory. *Journal of Structural Geology*, 22(7), 865–879. [https://doi.org/10.1016/S0191-](https://doi.org/10.1016/S0191-8141(00)00011-0)
781 [8141\(00\)00011-0](https://doi.org/10.1016/S0191-8141(00)00011-0)

782 Gupta, S., Underbill, J. R., Sharp, I. R., & Gawthorpe, R. L. (1999). Role of fault interactions in
783 controlling synrift sediment dispersal patterns: Miocene, Abu Alaqa Group, Suez Rift, Sinai,

784 Egypt. *Basin Research*, 11(2), 167–189. <https://doi.org/10.1046/j.1365-2117.1999.00300.x>

785 Hardy, S., & McClay, K. (1999). Kinematic modelling of extensional fault-propagation folding.
786 *Journal of Structural Geology*, 21(7), 695–702. [https://doi.org/10.1016/S0191-](https://doi.org/10.1016/S0191-8141(99)00072-3)
787 [8141\(99\)00072-3](https://doi.org/10.1016/S0191-8141(99)00072-3)

788 Harishidayat, D., Omosanya, K. O., & Johansen, S. E. (2015). 3D seismic interpretation of the
789 depositional morphology of the Middle to Late Triassic fluvial system in Eastern
790 Hammerfest Basin, Barents Sea. *Marine and Petroleum Geology*, 68(November 2017),
791 470–479. <https://doi.org/10.1016/j.marpetgeo.2015.09.007>

792 Iacopini, D., Butler, R. W. H., Purves, S., McArdle, N., & De Freslon, N. (2016). Exploring the
793 seismic expression of fault zones in 3D seismic volumes. *Journal of Structural Geology*, 89,
794 54–73. <https://doi.org/10.1016/j.jsg.2016.05.005>

795 Indrevær, K., Bergh, S. G., Koehl, J. B., Hansen, J. A., Schermer, E. R., & Ingebrigtsen, A. (2013).
796 Post-Caledonian brittle fault zones on the hyperextended SW Barents Sea margin: New
797 insights into onshore and offshore margin architecture. *Norsk Geologisk Tidsskrift*, 93(3–4),
798 167–188.

799 Jackson, C. A.L., & Larsen, E. (2009). Temporal and spatial development of a gravity-driven
800 normal fault array: Middle-Upper Jurassic, South Viking Graben, northern North Sea.
801 *Journal of Structural Geology*, 31(4), 388–402. <https://doi.org/10.1016/j.jsg.2009.01.007>

802 Jackson, Christopher A.L., & Lewis, M. M. (2016). Structural style and evolution of a salt-
803 influenced rift basin margin; the impact of variations in salt composition and the role of

804 polyphase extension. *Basin Research*, 28(1), 81–102. <https://doi.org/10.1111/bre.12099>

805 Jackson, Christopher A.L., & Rotevatn, A. (2013). 3D seismic analysis of the structure and
806 evolution of a salt-influenced normal fault zone: A test of competing fault growth models.
807 *Journal of Structural Geology*, 54, 215–234. <https://doi.org/10.1016/j.jsg.2013.06.012>

808 Jackson, Christopher A.L., Bell, R. E., Rotevatn, A., & Tvedt, A. B. M. (2017). Techniques to
809 determine the kinematics of synsedimentary normal faults and implications for fault
810 growth models. *Geological Society Special Publication*, 439(1), 187–217.
811 <https://doi.org/10.1144/SP439.22>

812 Jackson, Christopher A.L., Whipp, P. S., Gawthorpe, R. L., & Lewis, M. M. (2020). Structure and
813 kinematics of an extensional growth fold, Hadahid Fault System, Suez Rift, Egypt. *Solid*
814 *Earth*, 11(3), 1027–1051. <https://doi.org/10.5194/se-11-1027-2020>

815 Jackson, J. A. (1987). Active normal faulting and crustal extension. *Geological Society Special*
816 *Publication*, 28(28), 3–17. <https://doi.org/10.1144/GSL.SP.1987.028.01.02>

817 Johansen, S. E., Ostisty, B. K., Birkeland, Fedorovsky, Y. F., Martirosjan, V. N., Christensen, O. B.,
818 Cheredeev, S. I., Ignatenko, E. A., & Margulis, L. S. (1993). Hydrocarbon potential in the
819 Barents Sea region: Play distribution and potential. In Norwegian Petroleum Society
820 Special Publications (Vol. 2, Issue C, pp. 273–320). Elsevier. [https://doi.org/10.1016/B978-](https://doi.org/10.1016/B978-0-444-88943-0.50024-1)
821 [0-444-88943-0.50024-1](https://doi.org/10.1016/B978-0-444-88943-0.50024-1)

822 Kane, K. E., Jackson, C. A. L., & Larsen, E. (2010). Normal fault growth and fault-related folding
823 in a salt-influenced rift basin: South Viking Graben, offshore Norway. *Journal of Structural*

824 *Geology*, 32(4), 490–506. <https://doi.org/10.1016/j.jsg.2010.02.005>

825 Khalil, S. M., & McClay, K. R. (2002). Extensional fault-related folding, northwestern Red Sea,
826 Egypt. *Journal of Structural Geology*, 24(4), 743–762. [https://doi.org/10.1016/S0191-](https://doi.org/10.1016/S0191-8141(01)00118-3)
827 [8141\(01\)00118-3](https://doi.org/10.1016/S0191-8141(01)00118-3)

828 Khalil, Samir M., & McClay, K. R. (2017). 3D geometry and kinematic evolution of extensional
829 fault-related folds, NW Red Sea, Egypt. *Geological Society Special Publication*, 439(1), 109–
830 130. <https://doi.org/10.1144/SP439.11>

831 Khalil, Samir M., & McClay, K. R. (2018). Extensional fault-related folding in the northwestern
832 red sea, egypt: Segmented fault growth, fault linkages, corner folds and basin evolution.
833 *Geological Society Special Publication*, 476(1), 49–81. <https://doi.org/10.1144/SP476.12>

834 Lăpădat, A., Imber, J., Yielding, G., Iacopini, D., McCaffrey, K. J. W., Long, J. J., & Jones, R. R.
835 (2017). Occurrence and development of folding related to normal faulting within a
836 mechanically heterogeneous sedimentary sequence: A case study from Inner Moray Firth,
837 UK. *Geological Society Special Publication*, 439(1), 373–394.
838 <https://doi.org/10.1144/SP439.18>

839 Larssen, G. B., Elvebakk, G., Henriksen, L. B., Nilsson, I., Samuelsen, T. J., Stemmerik, L.,
840 Worsley, D., Kristensen, S. E., & Svånå, T. a. (2002). Upper Palaeozoic lithostratigraphy of
841 the Southern Norwegian Barents Sea. *Norwegian Petroleum Directorate Bulletin*, 9, 76.

842 Laubscher, H., 1982. Die Sudostecke des Rheingrabens-ein kinematisches und dyna- misches
843 problem. *Ecolgae Geologicae Helvetiae*, 75 (1), 101–116.

844 Lewis, M. M., Jackson, C. A. L., & Gawthorpe, R. L. (2013). Salt-influenced normal fault growth
845 and forced folding: The Stavanger Fault System, North Sea. *Journal of Structural Geology*,
846 54, 156–173. <https://doi.org/10.1016/j.jsg.2013.07.015>

847 Lewis, M. M., Jackson, C. A. L., Gawthorpe, R. L., & Whipp, P. S. (2015). Early synrift reservoir
848 development on the flanks of extensional forced folds: A seismic-scale outcrop analog
849 from the Hadahid fault system, Suez rift, Egypt. *AAPG Bulletin*, 99(6), 985–1012.
850 <https://doi.org/10.1306/12011414036>

851 Long, J. J., & Imber, J. (2010). Geometrically coherent continuous deformation in the volume
852 surrounding a seismically imaged normal fault-array. *Journal of Structural Geology*, 32(2),
853 222–234. <https://doi.org/10.1016/j.jsg.2009.11.009>

854 Mansfield, C. S., & Cartwright, J. A. (1996). High resolution fault displacement mapping from
855 three-dimensional seismic data: Evidence for dip linkage during fault growth. *Journal of*
856 *Structural Geology*, 18(2–3), 249–263. [https://doi.org/10.1016/S0191-8141\(96\)80048-4](https://doi.org/10.1016/S0191-8141(96)80048-4)

857 Mansfield, C. S., & Cartwright, J. A. (2000). Stratal fold patterns adjacent to normal faults:
858 Observations from the Gulf of Mexico. *Geological Society Special Publication*, 169, 115–
859 128. <https://doi.org/10.1144/GSL.SP.2000.169.01.09>

860 Mattos, N. H., Alves, T. M., & Omosanya, K. O. (2016). Crestal fault geometries reveal late
861 halokinesis and collapse of the Samson Dome, Northern Norway: Implications for
862 petroleum systems in the Barents Sea. *Tectonophysics*, 690, 76–96.
863 <https://doi.org/10.1016/j.tecto.2016.04.043>

864 Maurin, J.-C., & Niviere, B. (1999). Extensional forced folding and décollement of the pre-rift
865 series along the Rhine graben and their influence on the geometry of the syn-rift
866 sequences. Geological Society, London, Special Publications, 169(1), 73 LP – 86.
867 <https://doi.org/10.1144/GSL.SP.2000.169.01.06>

868 McClay, K. R., & Scott, A. D. (1991). Experimental models of hangingwall deformation in ramp-
869 flat listric extensional fault systems. *Tectonophysics*, 188(1), 85–96.

870 McHarg, S., Elders, C., & Cunneen, J. (2020). Extensional fault-related folding of the North West
871 shelf, Western Australia. AAPG Bulletin, 104(4), 913–938.
872 <https://doi.org/10.1306/08301918030>

873 McLeod, A. E., Dawers, N. H., & Underhill, J. R. (2000). The propagation and linkage of normal
874 faults: Insights from the Strathspey-Brent-Stafjord fault array, Northern North Sea. *Basin*
875 *Research*, 12(3–4), 263–284. <https://doi.org/10.1111/j.1365-2117.2000.00124.x>

876 Michie, E. A. H., Mulrooney, M. J., & Braathen, A. (2021). Fault Interpretation Uncertainties
877 using Seismic Data, and the Effects on Fault Seal Analysis: A Case Study from the Horda
878 Platform, with Implications for CO₂ storage. *Solid Earth Discussions*, 2021, 1–46.
879 <https://doi.org/10.5194/se-2021-23>

880 Mohammedyasin, S. M., Lippard, S. J., Omosanya, K. O., Johansen, S. E., & Harishidayat, D.
881 (2016). Deep-seated faults and hydrocarbon leakage in the Snøhvit Gas Field, Hammerfest
882 Basin, Southwestern Barents Sea. *Marine and Petroleum Geology*, 77, 160–178.
883 <https://doi.org/10.1016/j.marpetgeo.2016.06.011>

884 Morley, C. K. (1999). Patterns of displacement along large normal faults: Implications for basin
885 evolution and fault propagation, based on examples from east Africa. *AAPG Bulletin*
886 (*American Association of Petroleum Geologists*), 83(4), 613–634.
887 <https://doi.org/10.1306/00aa9c0a-1730-11d7-8645000102c1865d>

888 Morley, C. K. (2002). Evolution of Large Normal Faults: Evidence from Seismic Reflection Data.
889 *AAPG Bulletin*, 86(6), 961–978. [https://doi.org/10.1306/61EEDBFC-173E-11D7-](https://doi.org/10.1306/61EEDBFC-173E-11D7-8645000102C1865D)
890 [8645000102C1865D](https://doi.org/10.1306/61EEDBFC-173E-11D7-8645000102C1865D)

891 Patton, T. L. (2004). Numerical models of growth-sediment development above an active
892 monocline. *Basin Research*, 16(1), 25–39. [https://doi.org/10.1111/j.1365-](https://doi.org/10.1111/j.1365-2117.2003.00220.x)
893 [2117.2003.00220.x](https://doi.org/10.1111/j.1365-2117.2003.00220.x)

894 Peacock, D. C. P. (2002). Propagation, interaction and linkage in normal fault systems. *Earth-*
895 *Science Reviews*, 58(1–2), 121–142. [https://doi.org/10.1016/S0012-8252\(01\)00085-X](https://doi.org/10.1016/S0012-8252(01)00085-X)

896 Peacock, D. C. P., & Sanderson, D. J. (1991). Displacements, segment linkage and relay ramps in
897 normal fault zones. *Journal of Structural Geology*, 13(6), 721–733.
898 [https://doi.org/10.1016/0191-8141\(91\)90033-F](https://doi.org/10.1016/0191-8141(91)90033-F)

899 Prosser, S. (1993). Rift-related linked depositional systems and their seismic expression.
900 Geological Society, London, Special Publications, 71(1), 35 LP – 66.

901 Randen, T., Pedersen, S. I., & Sønneland, L. (2001). Automatic extraction of fault surfaces from
902 three-dimensional seismic data. *SEG Technical Program Expanded Abstracts*, 20(1), 551–
903 554. <https://doi.org/10.1190/1.1816675>

904 Ritzmann, O., & Faleide, J. I. (2007). Caledonian basement of the western Barents Sea.
905 *Tectonics*, 26(5), 1–20. <https://doi.org/10.1029/2006TC002059>

906 Roche, V., Camanni, G., Childs, C., Manzocchi, T., Walsh, J., Conneally, J., Saqab, M. M., &
907 Delogkos, E. (2021). Variability in the three-dimensional geometry of segmented normal
908 fault surfaces. *Earth-Science Reviews*, 103523.
909 <https://doi.org/10.1016/j.earscirev.2021.103523>

910 Roche, V., Childs, C., Madritsch, H., & Camanni, G. (2020). Layering and structural inheritance
911 controls on fault zone structure in three dimensions: A case study from the northern
912 Molasse basin, Switzerland. *Journal of the Geological Society*, 177(3), 493–508.
913 <https://doi.org/10.1144/jgs2019-052>

914 Rotevatn, A., & Jackson, C. A.-L. (2014). 3D structure and evolution of folds during normal fault
915 dip linkage. *Journal of the Geological Society*, 171(6), 821 LP – 829.
916 <https://doi.org/10.1144/jgs2014-045>

917 Rykkelid, E., & Fossen, H. (2002). Layer rotation around vertical fault overlap zones:
918 Observations from seismic data, field examples, and physical experiments. *Marine and*
919 *Petroleum Geology*, 19(2), 181–192. [https://doi.org/10.1016/S0264-8172\(02\)00007-7](https://doi.org/10.1016/S0264-8172(02)00007-7)

920 Schlische, R. W. (1992). Structural and stratigraphic development of the Newark extensional
921 basin, eastern North America: evidence for the growth of the basin and its bounding
922 structures. *Geological Society of America Bulletin*, 104(10), 1246–1263.
923 [https://doi.org/10.1130/0016-7606\(1992\)104<1246:SASDOT>2.3.CO;2](https://doi.org/10.1130/0016-7606(1992)104<1246:SASDOT>2.3.CO;2)

- 924 Schlische, R. W. (1995). Geometry and origin of fault-related folds in extensional settings.
925 American Association of Petroleum Geologists Bulletin, 79(11), 1661–1678.
926 <https://doi.org/10.1306/7834de4a-1721-11d7-8645000102c1865d>
- 927 Schöpfer, M. P. J., Childs, C., & Walsh, J. J. (2006). Localisation of normal faults in multilayer
928 sequences. *Journal of Structural Geology*, 28(5), 816–833.
929 <https://doi.org/10.1016/j.jsg.2006.02.003>
- 930 Schöpfer, M. P. J., Childs, C., Walsh, J. J., Manzcchi, T., & Koyi, H. A. (2007). Geometrical
931 analysis of the refraction and segmentation of normal faults in periodically layered
932 sequences. *Journal of Structural Geology*, 29(2), 318–335.
933 <https://doi.org/https://doi.org/10.1016/j.jsg.2006.08.006>
- 934 Sharp, I. R., Gawthorpe, R. L., Underhill, J. R., & Gupta, S. (2000). Fault-propagation folding in
935 extensional settings: Examples of structural style and synrift sedimentary response from
936 the Suez rift, Sinai, Egypt. *Bulletin of the Geological Society of America*, 112(12), 1877–
937 1899. [https://doi.org/10.1130/0016-7606\(2000\)112<1877:FPFIES>2.0.CO;2](https://doi.org/10.1130/0016-7606(2000)112<1877:FPFIES>2.0.CO;2)
- 938 Smart, K. J., & Ferrill, D. A. (2018). Discrete element modeling of extensional fault-related
939 monocline formation. *Journal of Structural Geology*, 115, 82–90.
940 <https://doi.org/https://doi.org/10.1016/j.jsg.2018.07.009>
- 941 Tavani, S., Balsamo, F., & Granado, P. (2018). Petroleum system in supra-salt strata of
942 extensional forced-folds: A case-study from the Basque-Cantabrian basin (Spain). *Marine
943 and Petroleum Geology*, 96(June), 315–330.

944 <https://doi.org/10.1016/j.marpetgeo.2018.06.008>

945 Taylor, S. K., Nicol, A., & Walsh, J. J. (2008). Displacement loss on growth faults due to sediment
946 compaction. *Journal of Structural Geology*, 30(3), 394–405.

947 <https://doi.org/10.1016/j.jsg.2007.11.006>

948 Torabi, A., Alaei, B., & Libak, A. (2019). Normal fault 3D geometry and displacement revisited:
949 Insights from faults in the Norwegian Barents Sea. *Marine and Petroleum Geology*,
950 99(October 2018), 135–155. <https://doi.org/10.1016/j.marpetgeo.2018.09.032>

951 van der Zee, W., & Urai, J. L. (2005). Processes of normal fault evolution in a siliciclastic
952 sequence: A case study from Miri, Sarawak, Malaysia. *Journal of Structural Geology*,
953 27(12), 2281–2300. <https://doi.org/10.1016/j.jsg.2005.07.006>

954 Walsh, J. J., & Watterson, J. (1991). Geometric and kinematic coherence and scale effects of
955 normal fault systems. In: *The Geometry of Normal Faults*, edited by: Roberts, A. M.,
956 Yielding, G., Freeman, B., Geol. Soc. Lond. Spec. Publ., 186, 157-170,
957 <https://doi.org/10.1144/GSL.SP.1991.056.01.13>

958 Walsh, J. J., Bailey, W. R., Childs, C., Nicol, A., & Bonson, C. G. (2003). Formation of segmented
959 normal faults: A 3-D perspective. *Journal of Structural Geology*, 25(8), 1251–1262.
960 [https://doi.org/10.1016/S0191-8141\(02\)00161-X](https://doi.org/10.1016/S0191-8141(02)00161-X)

961 Walsh, J. J., Nicol, A., & Childs, C. (2002). An alternative model for the growth of faults. *Journal*
962 *of Structural Geology*, 24(11), 1669–1675. [https://doi.org/10.1016/S0191-8141\(01\)00165-](https://doi.org/10.1016/S0191-8141(01)00165-1)
963 [1](https://doi.org/10.1016/S0191-8141(01)00165-1)

- 964 Walsh, J. J., Watterson, J., Bailey, W. R., & Childs, C. (1999). Fault relays, bends and branch-
965 lines. *Journal of Structural Geology*, 21(8–9), 1019–1026. [https://doi.org/10.1016/S0191-](https://doi.org/10.1016/S0191-8141(99)00026-7)
966 [8141\(99\)00026-7](https://doi.org/10.1016/S0191-8141(99)00026-7)
- 967 Walsh, J. J., Watterson, J., Childs, C., & Nicol, A. (1996). Ductile strain effects in the analysis of
968 seismic interpretations of normal fault systems. Geological Society, London, Special
969 Publications, 99(1), 27 LP – 40. <https://doi.org/10.1144/GSL.SP.1996.099.01.04>
- 970 White, I. R., & Crider, J. G. (2006). Extensional fault-propagation folds: mechanical models and
971 observations from the Modoc Plateau, northeastern California. *Journal of Structural*
972 *Geology*, 28(7), 1352–1370. <https://doi.org/10.1016/j.jsg.2006.03.028>
- 973 Willsey, S. P., Umhoefer, P. J., & Hilley, G. E. (2002). Early evolution of an extensional monocline
974 by a propagating normal fault: 3D analysis from combined field study and numerical
975 modeling. *Journal of Structural Geology*, 24(4), 651–669. [https://doi.org/10.1016/S0191-](https://doi.org/10.1016/S0191-8141(01)00120-1)
976 [8141\(01\)00120-1](https://doi.org/10.1016/S0191-8141(01)00120-1)
- 977 Withjack, M. O., & Callaway, S. (2000). Active normal faulting beneath a salt layer: An
978 experimental study of deformation patterns in the cover sequence. *AAPG Bulletin*, 84(5),
979 627–651. <https://doi.org/10.1306/c9ebce73-1735-11d7-8645000102c1865d>
- 980 Withjack, M. O., Henza, A. A., & Schlische, R. W. (2017). Three-dimensional fault geometries
981 and interactions within experimental models of multiphase extension. *AAPG Bulletin*,
982 101(11), 1767–1789. <https://doi.org/10.1306/02071716090>
- 983 Withjack, M. O., Olson, J., & Peterson, E. (1990). Experimental models of extensional forced

984 folds. American Association of Petroleum Geologists Bulletin, 74(7), 1038–1054.

985 <https://doi.org/10.1306/Oc9b23fd-1710-11d7-8645000102c1865d>

986 Young, M. J., Gawthorpe, R. L., & Hardy, S. (2001). Growth and linkage of a segmented normal
987 fault zone; the Late Jurassic Murchison-Statfjord North Fault, Northern North Sea. Journal
988 of Structural Geology, 23(12), 1933–1952. [https://doi.org/10.1016/S0191-8141\(01\)00038-](https://doi.org/10.1016/S0191-8141(01)00038-4)

989 [4](#)

990

991 Figure Captions

992 **Figure 1.** (a) Regional structural elements of SW Barents Sea. The green outline highlights the
993 location of the study area. The location of the studies used to further constrain seismic facies
994 and age relationships is noted by S1 (Mohammedyasin et al., 2016) and S2 (Harishidayat et al.,
995 2015 and Torabi et al., 2019). The red dashed line shows the location of the regional 2D cross
996 section shown in Fig 1b. The line brown line shows the present-day coastline of Norway.
997 Structural elements abbreviations (FH: Fedynsky High, VD: Veslekari Dome, NB: Nordkapp
998 Basin, NH: Norsel High, SG: Swaen Graben, MH: Mercurius High, SD: Samson Dome, LH: Loppa
999 High, HB: Hammerfest Basin, BF: Bjørnøyrenna Fault Complex, VH: Veslemøy High, SR: Senja
1000 Ridge, TFFC: Troms-Finnmark Fault Complex, MF: Måsøy Fault Complex, SB: Sørvestsnaget
1001 Basin, SH: Stappen High, BP: Bjarmeland Platform, TB: Tromsø Basin, FB: Finnmark Platform).
1002 The map is modified after information found in the Norwegian Petroleum Directorate fact page
1003 <http://www.npd.no/en/>. (b) Regional 2D seismic cross section showing the basin scale settings
1004 across The Finnmark Platform, Hammerfest Basin and Loppa High (modified from Gabrielsen,

1005 1984 and Mohammedyasin et al., 2016).

1006 **Figure 2.** Stratigraphic column for SW Barents Sea showing major tectonic events (modified
1007 after Gac et al., 2018 and Edmundson et al., 2019). The figure shows the major seismic horizons
1008 picked in the area and near the well location.

1009 **Figure 3.** Cartoon illustrations showing (a): how projected and observed throw cut-off points
1010 are picked to distinguish between throw due to tectonic subsidence alone and throw due to
1011 tectonic subsidence and deformation (modified after Duffy et al., 2015). (b): a degraded fault
1012 scarp.

1013

1014 **Figure 4.** (a.i): time slice at depth of 1400 ms that reveal the major fault systems in the study
1015 area using colour blending that combines tensor (yellow), dip (cyan) and semblance (magenta).
1016 (4.a.ii): a variance horizon slice extracted at the J4 level that shows the fault segments
1017 comprising the TFFC structure. (4.a.iii): interpreted fault systems using seismic attribute data
1018 above that shows the three fault systems within the study area. The red dotted line shows the
1019 composite seismic line location (Fig 4.c). The TFFC fault segments are labeled A-D. (4.b) Time
1020 structure maps of the base Permian-Carboniferous (4.b.i) and base Jurassic (4.b.ii) horizons.
1021 These horizons represent base syn-rift surfaces that corresponds to the 2nd and 3rd rift phases.
1022 The Blue dashed lines show the location of the seismic sections shown on Figs 5 & 6. The black
1023 dashed area represents the extent of the detailed horizon interpretation used in the fault
1024 kinematic analysis and Fig 10. (4.b.iii): interpreted structures from the base-Jurassic horizon.

1025 (4.c) Composite seismic line that highlights the structural variability between the three fault
1026 systems in the study area. Faults are colour-coded following the map legend in Fig 4a (Black:
1027 TFFC, Blue: E-W fault system, Maroon: ENE-WSW fault system). **Figure 5.** Interpreted seismic
1028 sections taken perpendicular to the strike of TFFC. These sections show the changes in fault
1029 patterns and deformation along the TFFC. Black arrows represent observed reflection
1030 terminations and red arrows highlight key onlap relationships in the sedimentary cover
1031 approaching the fault surface. The location of these sections is shown on Fig 4.b.i. The location
1032 of the sections in Fig 9 are shown on top of each respective section here.

1033 **Figure 6.** (a) Composite seismic line taken along strike of the TFFC. The line location is given in
1034 Fig. 4b.i. Location of seismic sections perpendicular to TFFC (Fig 5) are shown as black dashed
1035 lines and the location of the strike bends in the section are highlighted by black triangles above
1036 the section. TFFC fault segments are labelled A-D and shown above the interpreted composite
1037 seismic section (b). The location where the TFFC intersects this composite seismic section is
1038 shown on (b) by a red dashed line. (c) Time-structure maps for the P-C4 (i), T4 (ii), J4 (iii) and C4
1039 (iv) horizons are shown below the interpreted composite seismic line to show the fold
1040 development and distribution across different structural level.

1041 **Figure 7.** Throw-length profiles for horizons C4, J4, T4 and P-C4 (Lower Cretaceous, Lower
1042 Jurassic, Lower Triassic and Lower Permian of Upper Carboniferous). The blue line represents
1043 projected throw values while the red line shows the observe throw values. The difference
1044 between the two throw types is shaded in light yellow to represent ductile deformation. TFFC
1045 fault segments are marked by the green lines separating segments A – D from left to right.

1046 **Figure 8.** Strike-projected throw distributions along the TFFC surface for projected (a) and
1047 observed (b) throws. The two strike-projections show increased throw towards the NW part of
1048 the fault and local throw maximums along strike of the fault. The location of the local throw
1049 maximums coincides with the centre of each fault segment making the TFFC structure. The
1050 throw maximum the NW corresponds with a branchline that is interacting with the TFFC. The
1051 image on the right (c) shows the throw difference between projected and observed throws and
1052 represent the folding component along the TFFC, which is shown to be restricted in the
1053 sedimentary cover above basement. TFFC fault segments are marked by the green lines and
1054 annotated A – D respectively.

1055 **Figure 9.** Un-interpreted and interpreted, vertically exaggerated (x10) versions of the seismic
1056 sections shown in Fig.5 that highlight the folding and onlap relationships in the U. Triassic – u.
1057 Cretaceous stratigraphy.

1058 **Figure 10.** Isochrone maps superimposed on variance attribute surfaces (left) and interpretive
1059 sketches (right) for key stratigraphic units across the TFFC. The isochrone maps and
1060 accompanying sketches illustrate the thickness variations across the stratigraphic unit and
1061 constrain the timing of fault activity in the TFFC and adjacent faults. The location of individual
1062 TFFC fault segments is marked by the labelled circles A – D.

(a)

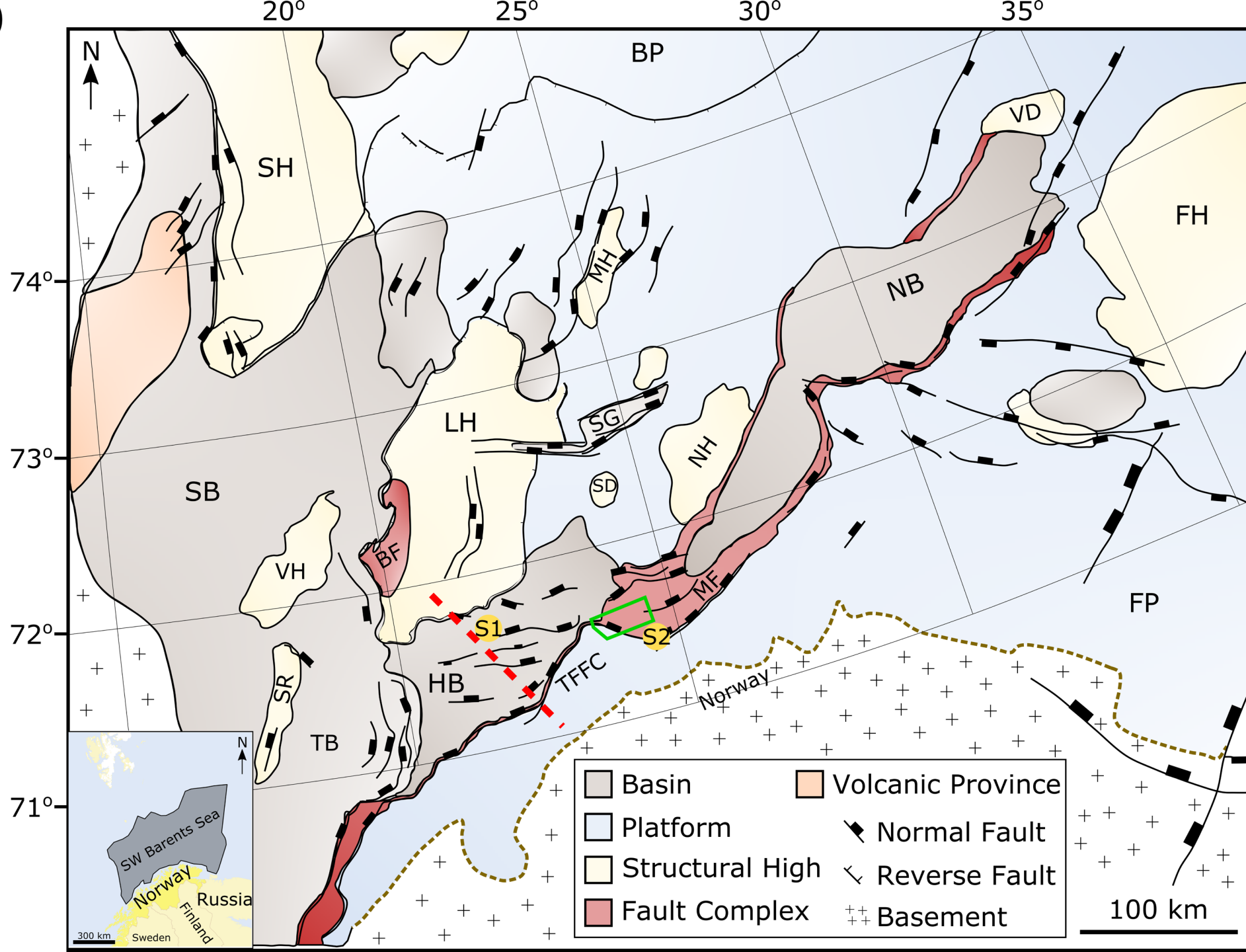
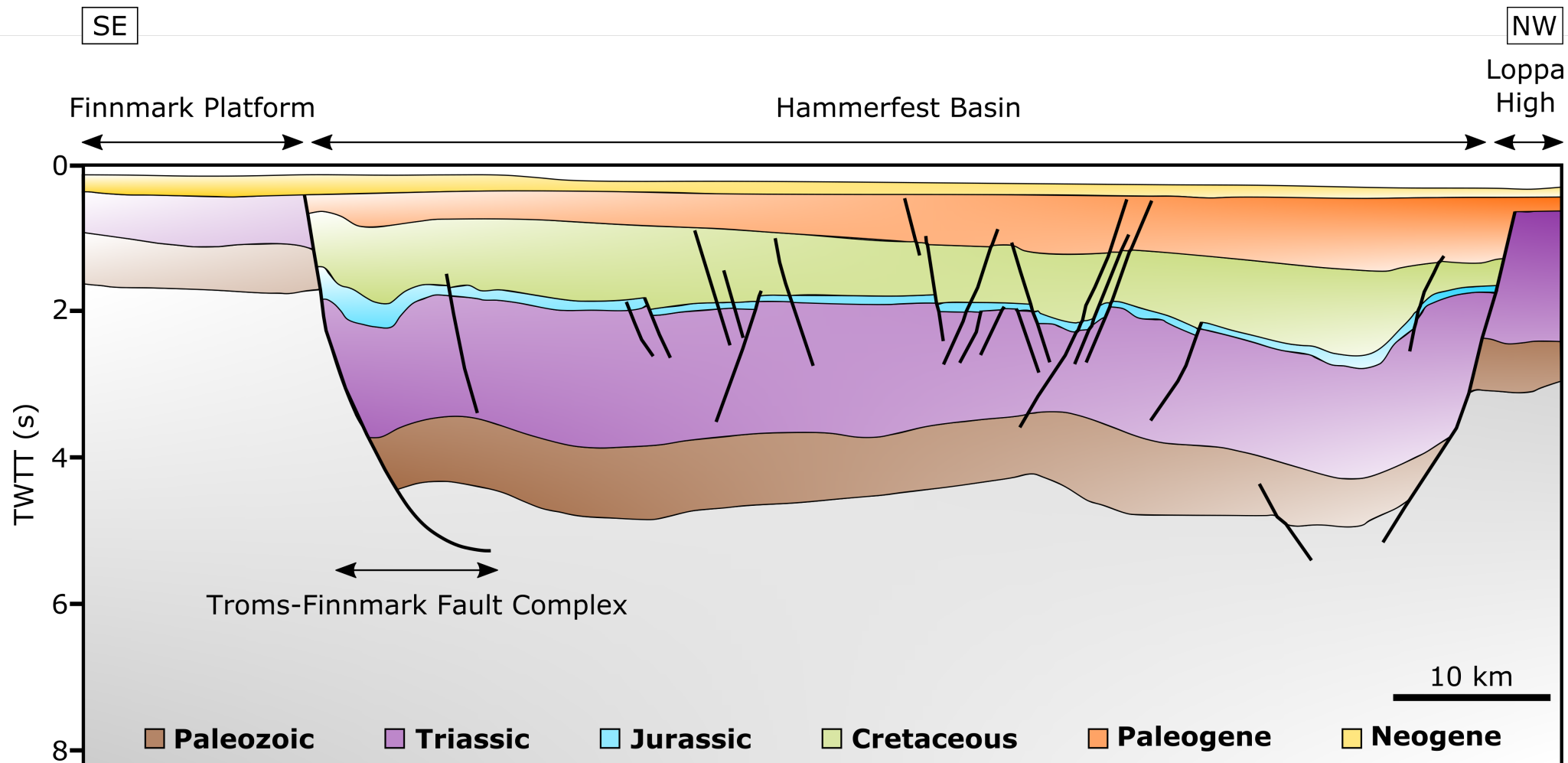
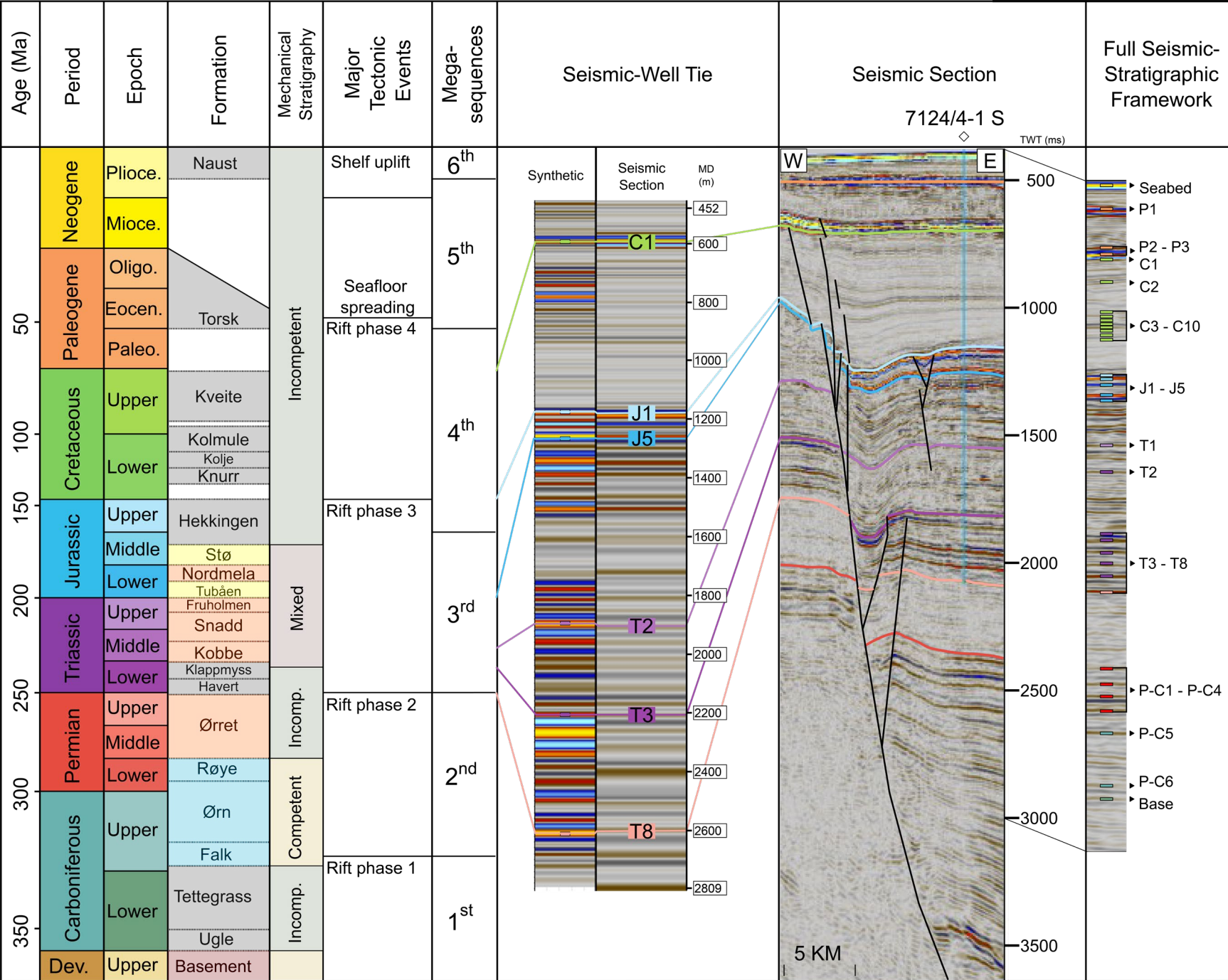


Figure 1. (a) Regional structural elements of SW Barents Sea. The green outline highlights the location of the study area. The location of the studies used to further constrain seismic facies and age relationships is noted by S1 (Mohammedyasin et al., 2016) and S2 (Harishidayat et al., 2015 and Torabi et al., 2019). The red dashed line shows the location of the regional 2D cross section shown in Fig 1b. The line brown line shows the present-day coastline of Norway. Structural elements abbreviations (FH: Fedynsky High, VD: Veslekari Dome, NB: Nordkapp Basin, NH: Norsel High, SG: Svaen Graben, MH: Mercurius High, SD: Samson Dome, LH: Loppa High, HB: Hammerfest Basin, BF: Bjørnøyrenna Fault Complex, VH: Veslemøy High, SR: Senja Ridge, TFFC: Troms-Finnmark Fault Complex, MF: Måsøy Fault Complex, SB: Sørvestsnaget Basin, SH: Stappen High, BP: Bjarmeland Platform, TB: Tromsø Basin, FB: Finnmark Platform). The map is modified after information found in the Norwegian Petroleum Directorate fact page <http://www.npd.no/en/>. (b) Regional 2D seismic cross section showing the basin scale settings across The Finnmark Platform, Hammerfest Basin and Loppa High (modified from Gabrielsen, 1984 and Mohammedyasin et al., 2016).

(b)

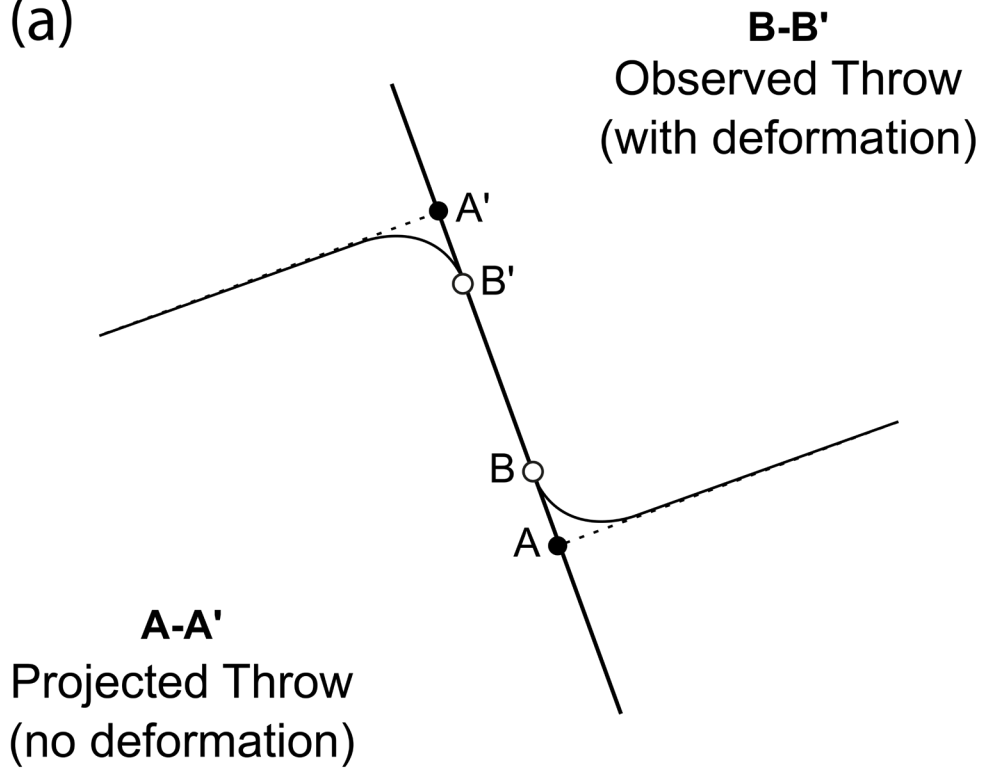




Crystalline Basement
 Mudstone
 Carbonates
 Siltstone
 Sandstone

Figure 2. Stratigraphic column for SW Barents Sea showing major tectonic events (modified after Gac et al., 2018 and Edmundson et al., 2019). The figure shows the major seismic horizons picked in the area and near the well location.

(a)



(b)

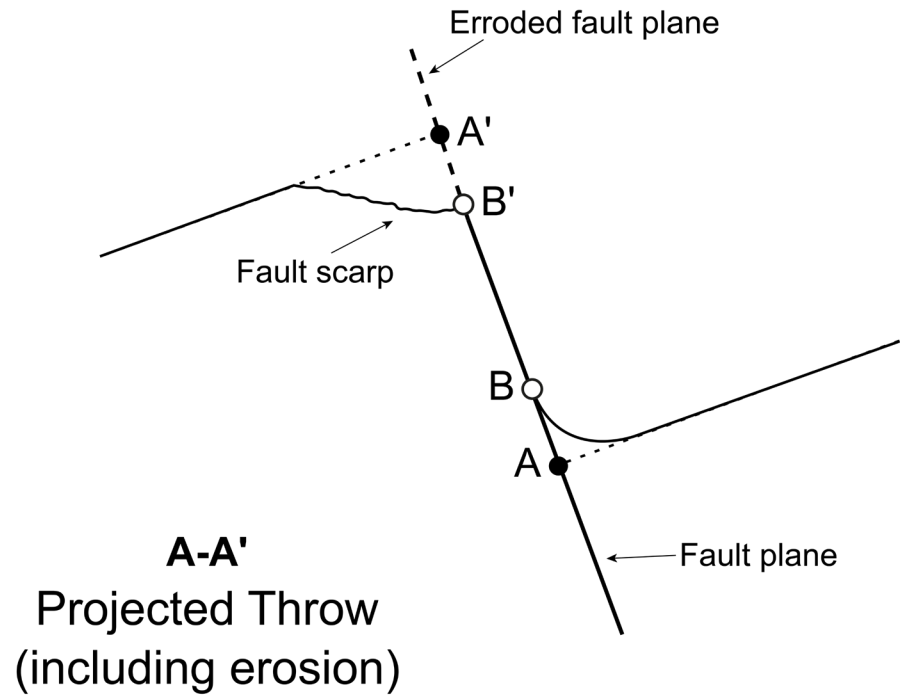
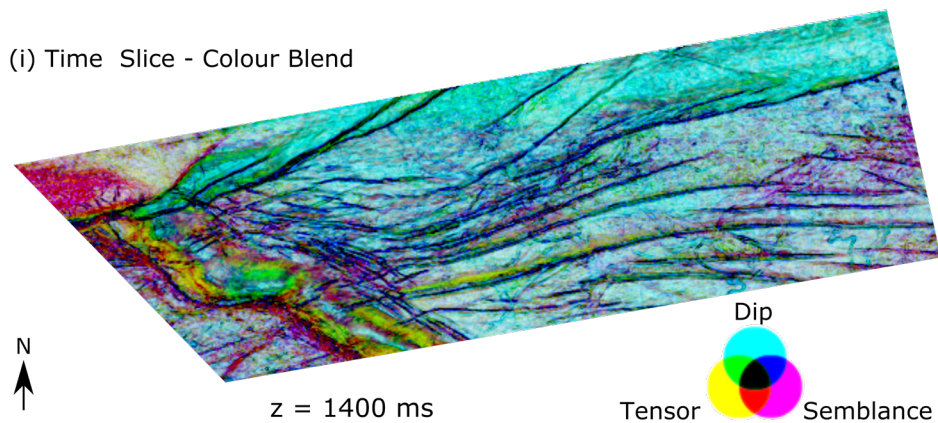
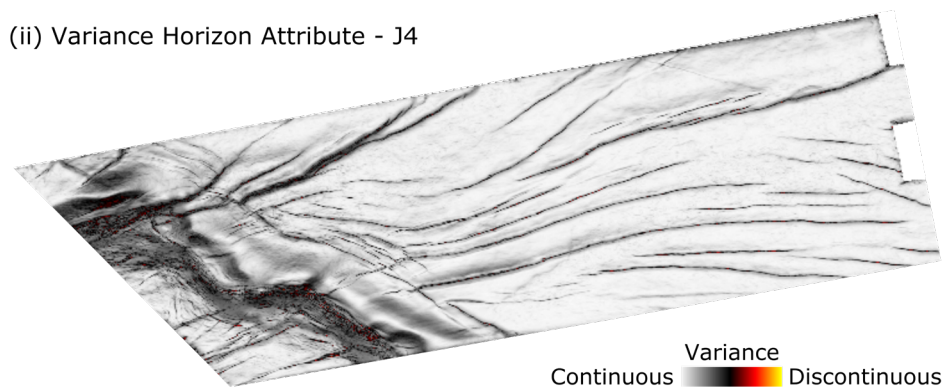
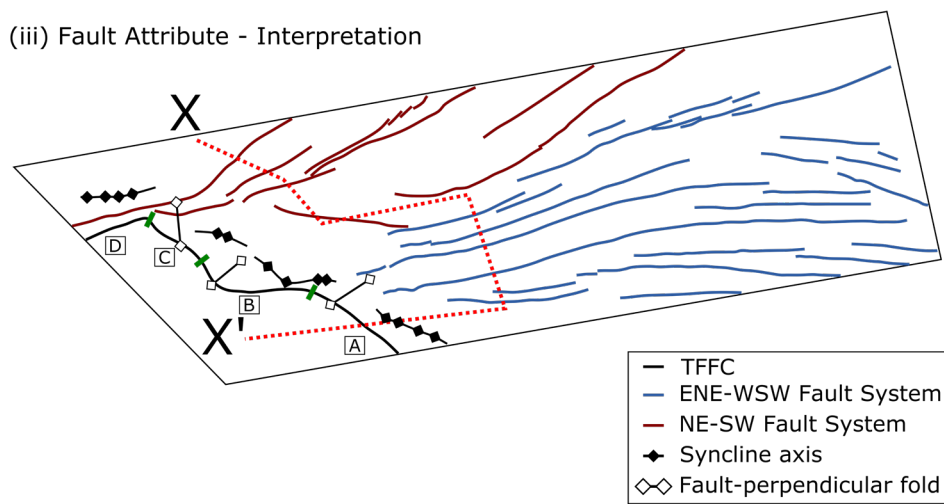
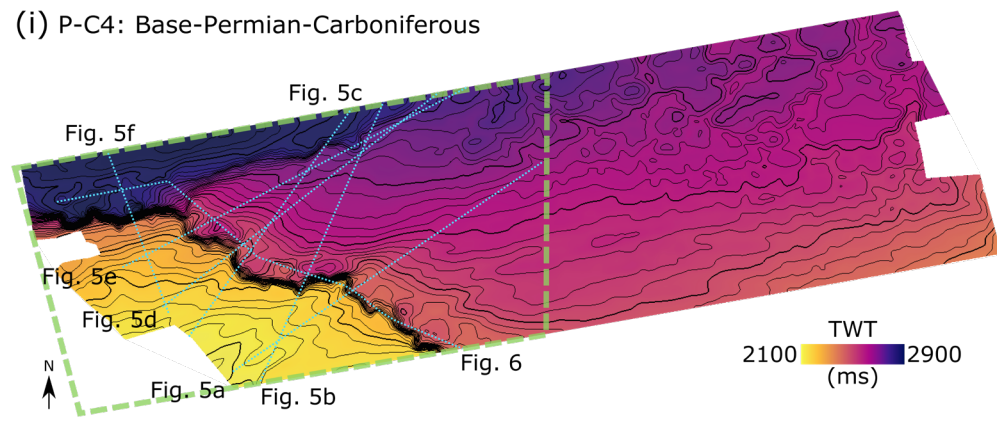
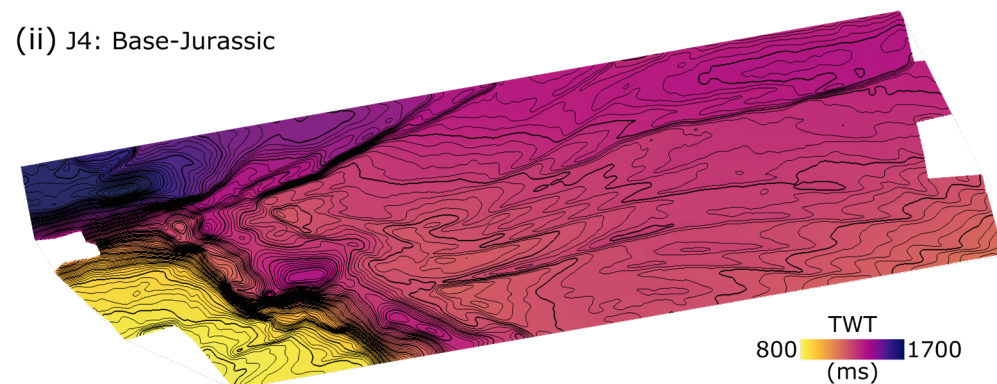
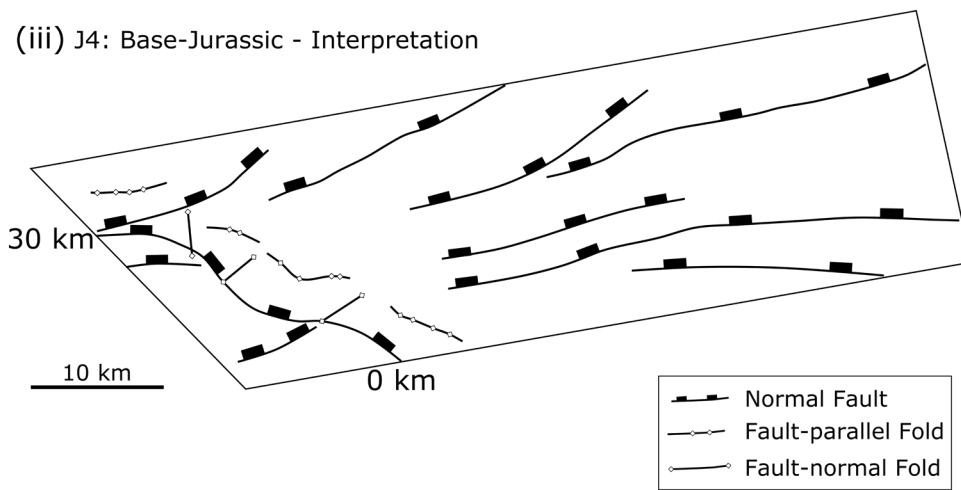


Figure 3. Cartoon illustrations showing (a): how projected and observed throw cut-off points are picked to distinguish between throw due to tectonic subsidence alone and throw due to tectonic subsidence and deformation (modified after Duffy et al., 2015). (b): a degraded fault scarp.

(a)**(i) Time Slice - Colour Blend****(ii) Variance Horizon Attribute - J4****(iii) Fault Attribute - Interpretation****(b)****(i) P-C4: Base-Permian-Carboniferous****(ii) J4: Base-Jurassic****(iii) J4: Base-Jurassic - Interpretation**

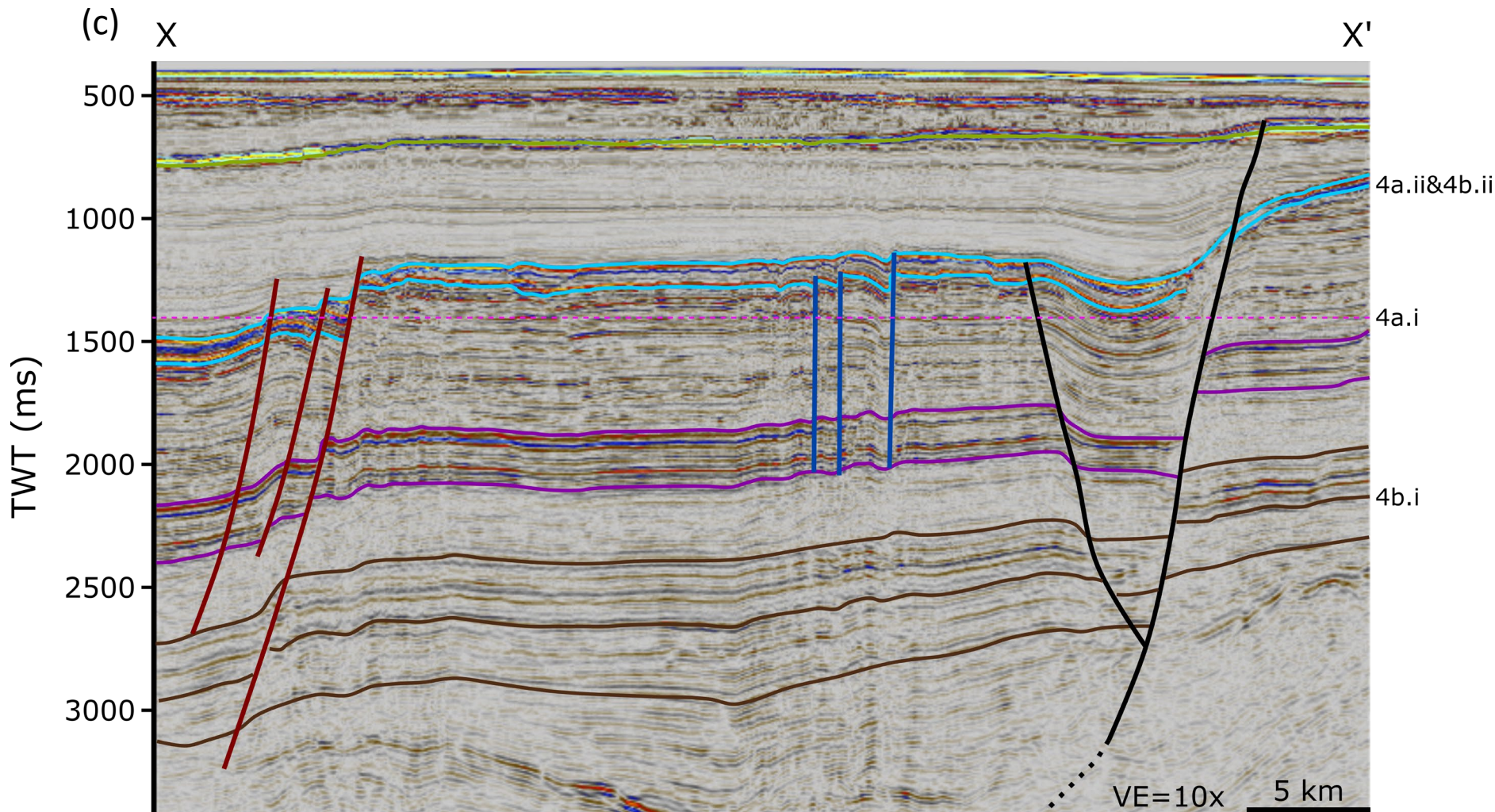


Figure 4. (a.i): time slice at depth of 1400 ms that reveal the major fault systems in the study area using colour blending that combines tensor (yellow), dip (cyan) and semblance (magenta). (4.a.ii): a variance horizon slice extracted at the J4 level that shows the fault segments comprising the TFFC structure. (4.a.iii): interpreted fault systems using seismic attribute data above that shows the three fault systems within the study area. The red dotted line shows the composite seismic line location (Fig 4.c). The TFFC fault segments are labeled A-D. (4.b) Time structure maps of the base Permian-Carboniferous (4.b.i) and base Jurassic (4.b.ii) horizons. These horizons represent base syn-rift surfaces that corresponds to the 2nd and 3rd rift phases. The Blue dashed lines show the location of the seismic sections shown on Figs 5 & 6. The black dashed area represents the extent of the detailed horizon interpretation used in the fault kinematic analysis and Fig 10. (4.b.iii): interpreted structures from the base-Jurassic horizon. (4.c) Composite seismic line that highlights the structural variability between the three fault systems in the study area. Faults are colour-coded following the map legend in Fig 4a (Black: TFFC, Blue: E-W fault system, Maroon: ENE-WSW fault system).

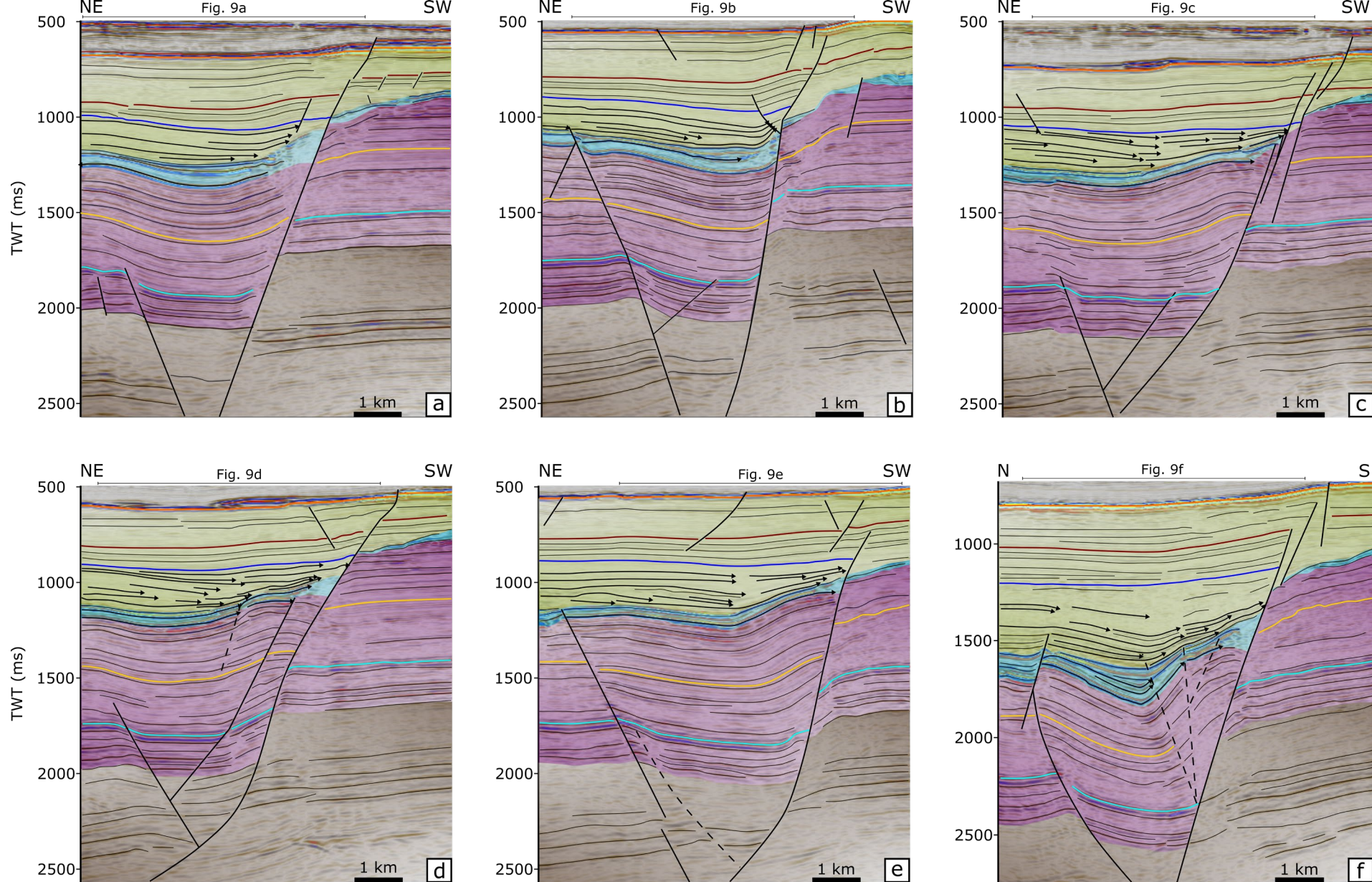


Figure 5. Interpreted seismic sections taken perpendicular to the strike of TFFC. These sections show the changes in fault patterns and deformation along the TFFC. Black arrows represent observed reflection terminations and red arrows highlight key onlap relationships in the sedimentary cover approaching the fault surface. The location of these sections is shown on Fig 4.b.i. The location of the sections in Fig 9 are shown on top of each respective section here.

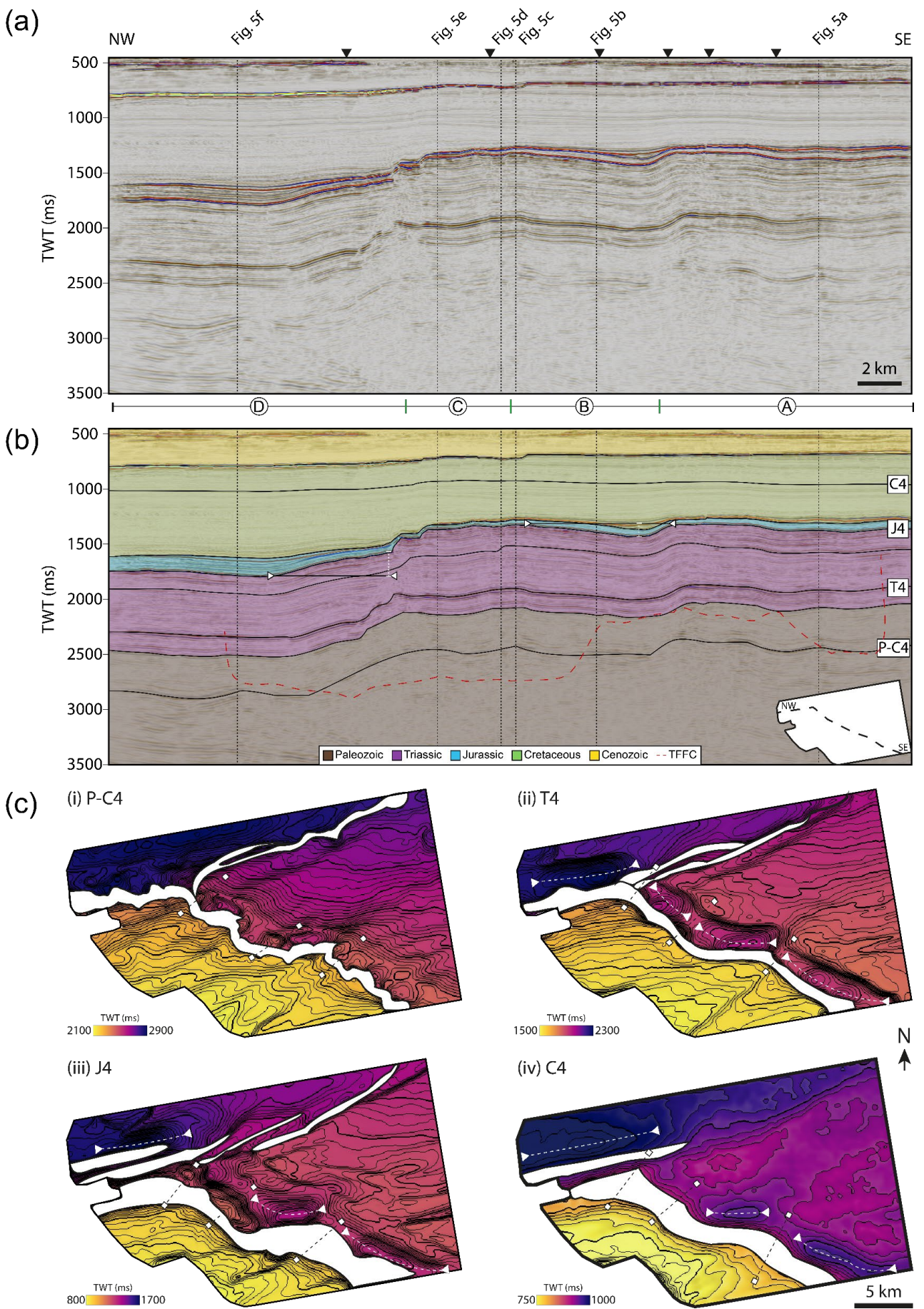


Figure 6. (a) Composite seismic line taken along strike of the TFFC. The line location is given in Fig. 4b.i. Location of seismic sections perpendicular to TFFC (Fig 5) are shown as black dashed lines and the location of the strike bends in the section are highlighted by black triangles above the section. TFFC fault segments are labelled A-D and shown above the interpreted composite seismic section (b). The location where the TFFC intersects this composite seismic section is shown on (b) by a red dashed line. (c) Time-structure maps for the P-C4 (i), T4 (ii), J4 (iii) and C4 (iv) horizons are shown below the interpreted composite seismic line to show the fold development and distribution across different structural level.

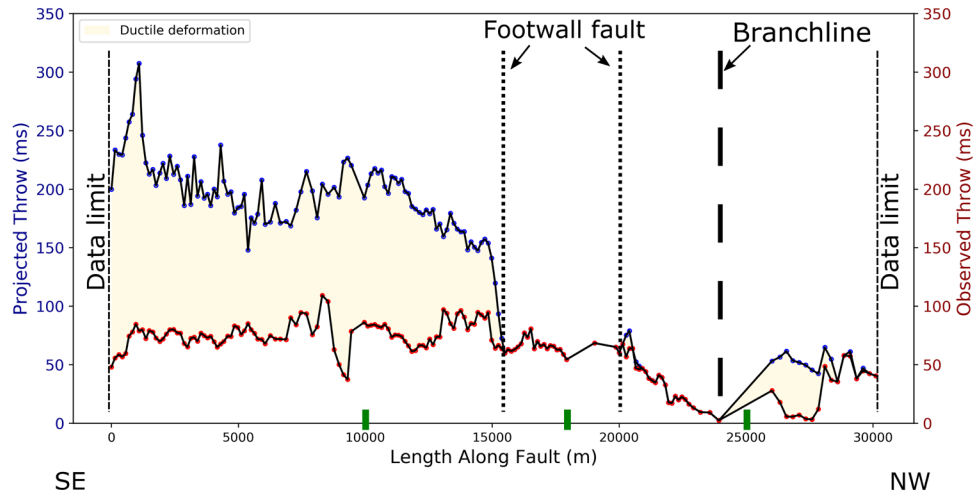
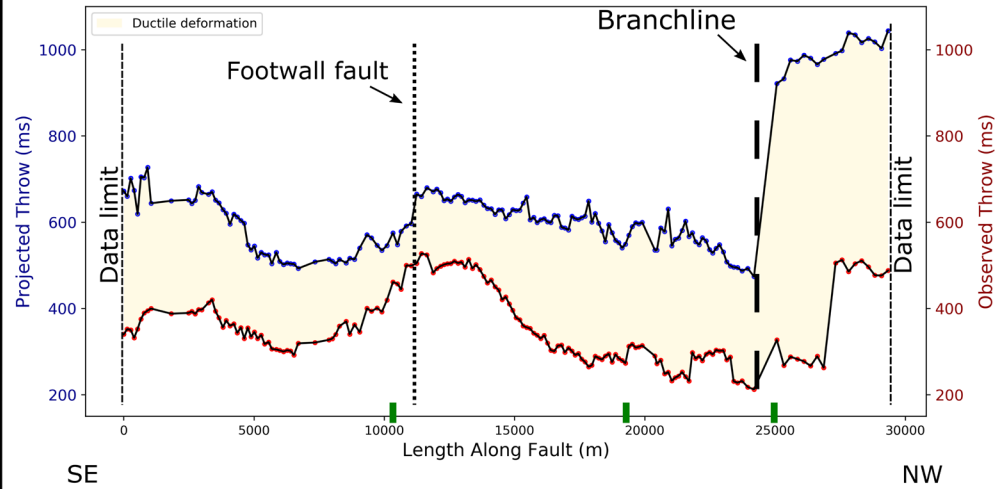
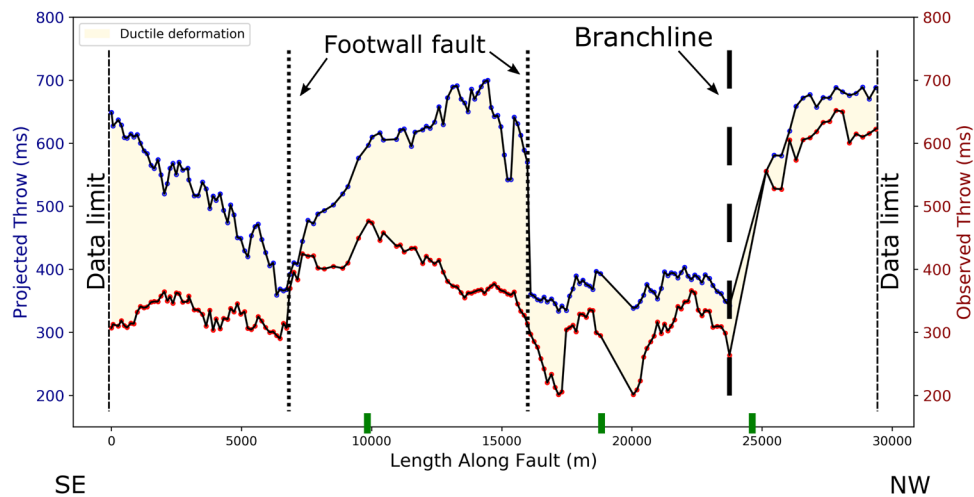
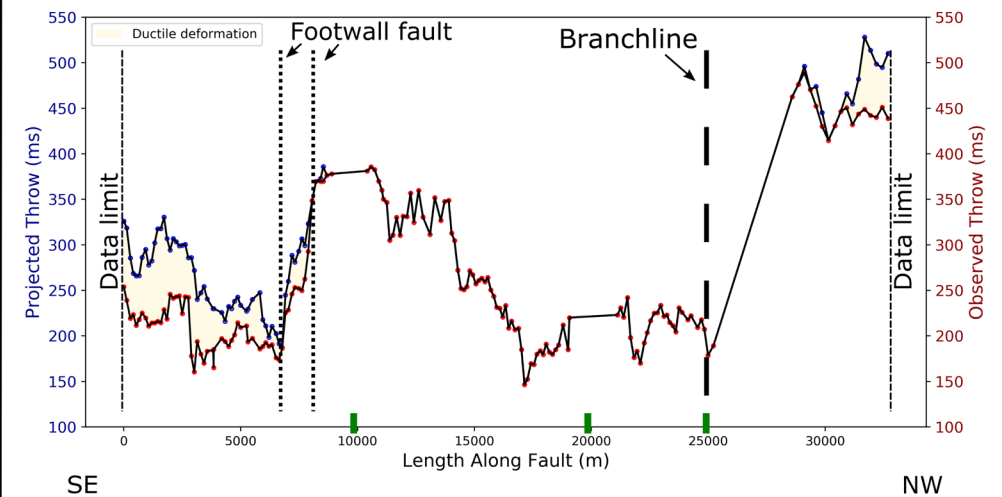
a L. Cretaceous (C4)**b** L. Jurassic (J4)**c** L. Triassic (T4)**d** L. Permian (P-C4)

Figure 7. Throw-length profiles of TFFC at stratigraphic levels of C4, J4, T4 and P-C4 (Lower Cretaceous, Lower Jurassic, Lower Triassic and Lower Permian of Upper Carboniferous). The blue line represents projected throw values while the red line shows the observed throw values. The difference between the two throw types is shaded in light yellow to represent ductile deformation. TFFC fault segments are marked by the green lines separating segments A – D from left to right.

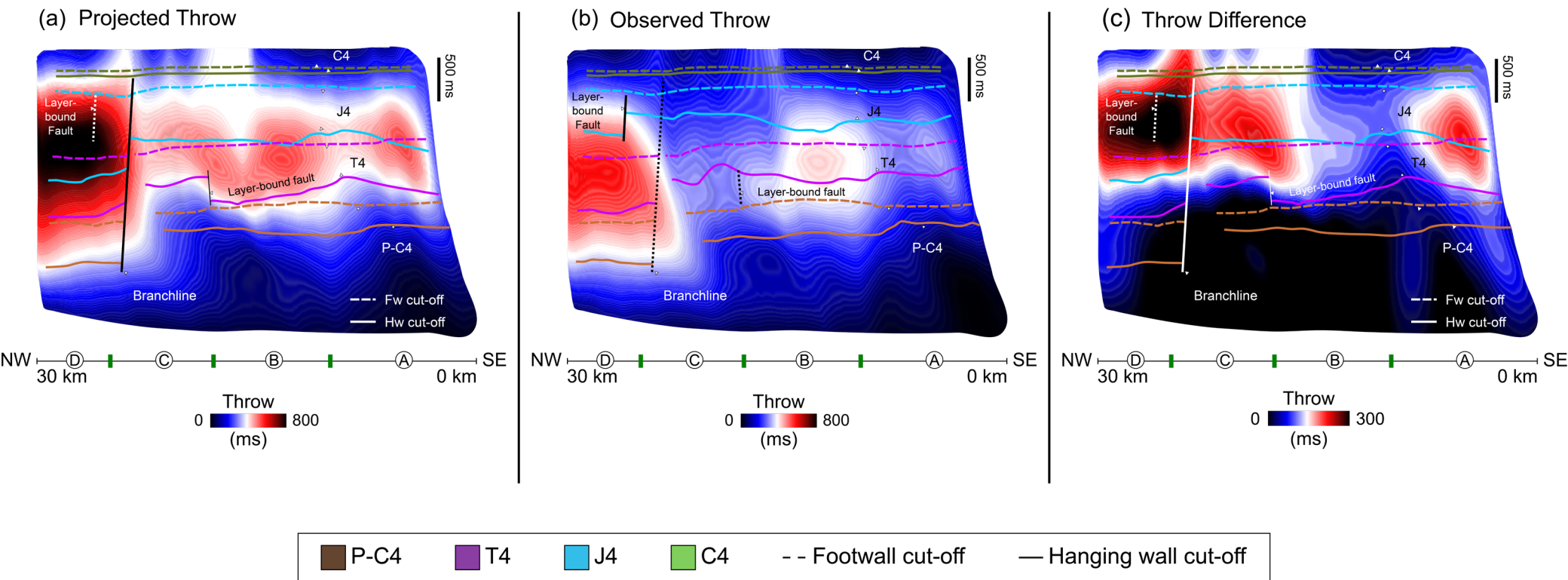


Figure 8. Strike-projected throw distributions along the TFFC surface for projected (a) and observed (b) throws. The two strike-projections show increased throw towards the NW part of the fault and local throw maximums along strike of the fault. The location of the local throw maximums coincides with the center of each fault segment making the TFFC structure. The throw maximum the NW corresponds with a branchline that is interacting with the TFFC. The image on the right (c) shows the throw difference between projected and observed throws and represent the folding component along the TFFC, which is shown to be restricted in the sedimentary cover above basement. TFFC fault segments are marked by the green lines and annotated A – D respectively.

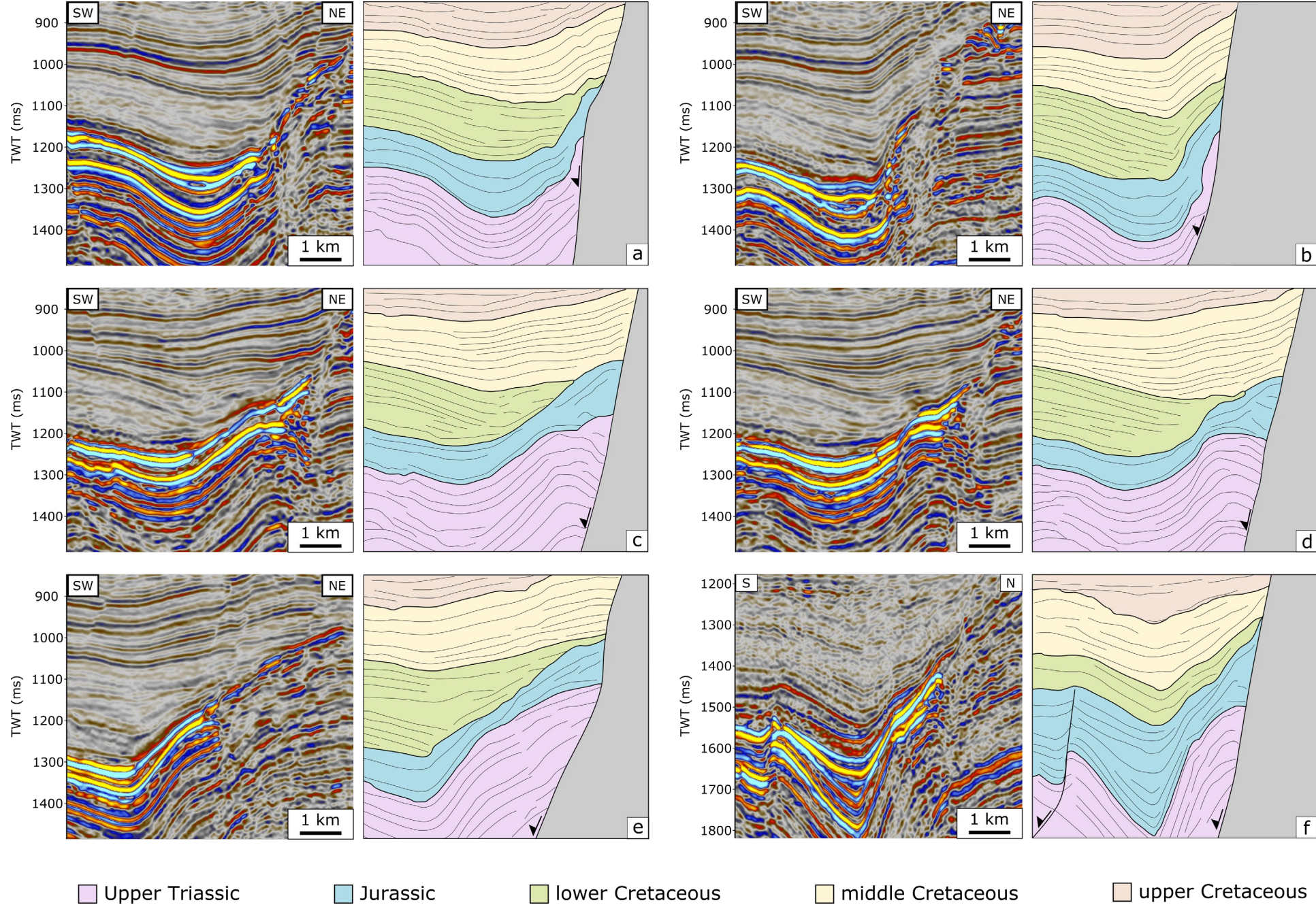
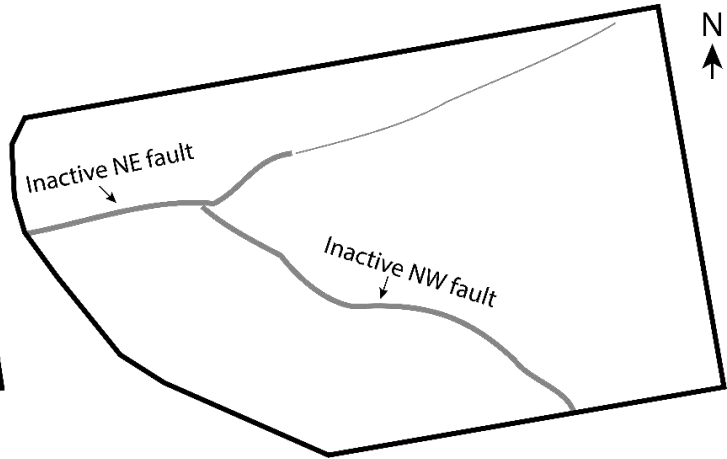
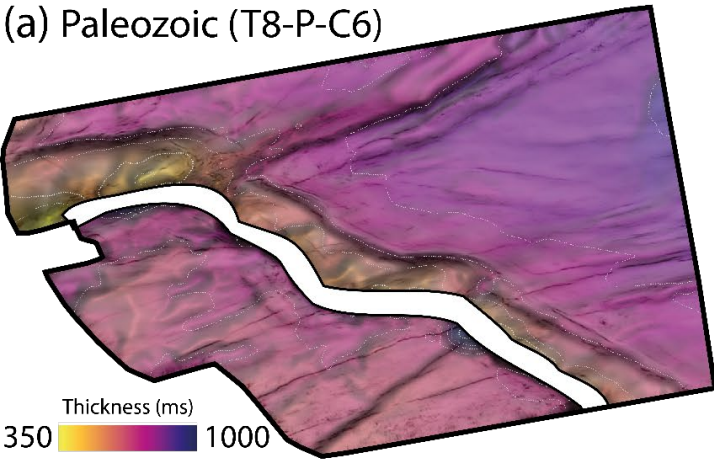
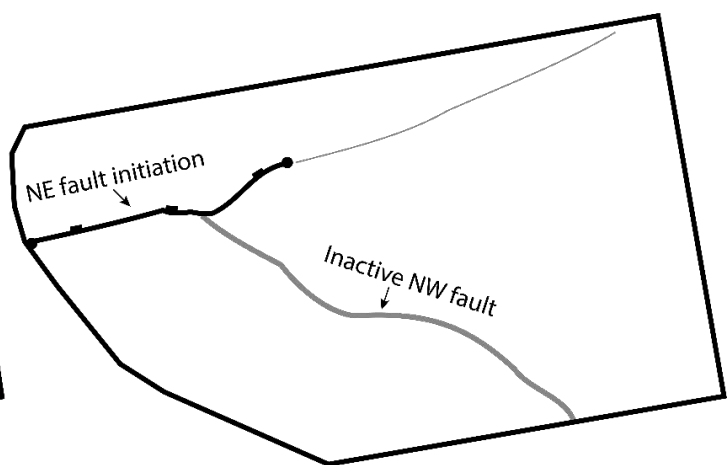
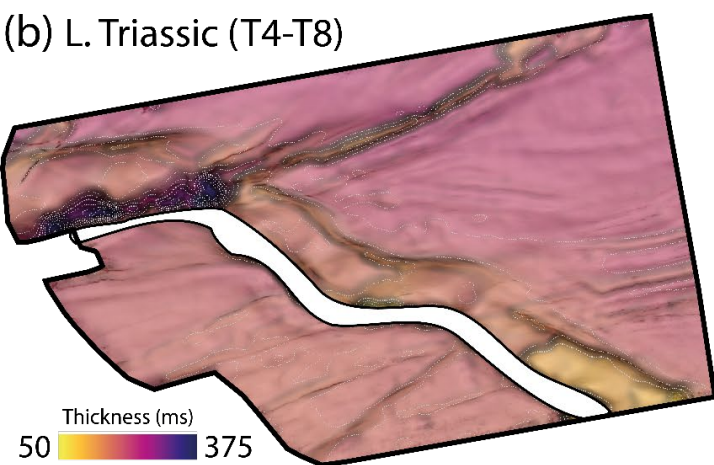


Figure 9. Un-interpreted and interpreted, vertically exaggerated (x10) versions of the seismic sections shown in Fig.5 that highlight the folding and onlap relationships in the U. Triassic – U. Cretaceous stratigraphy in the hanging wall of the TFFC.

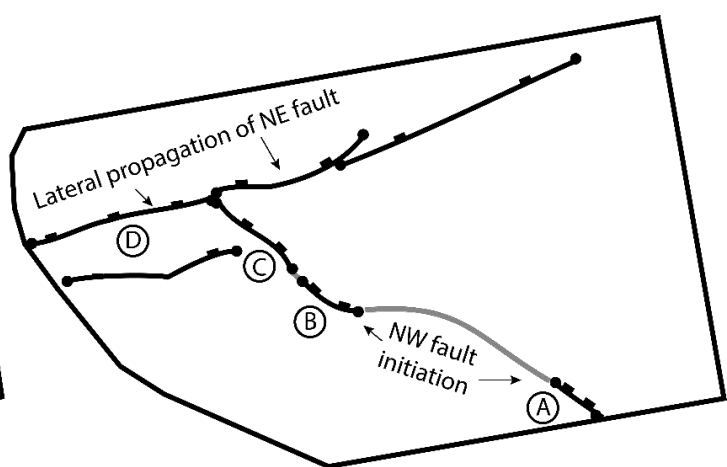
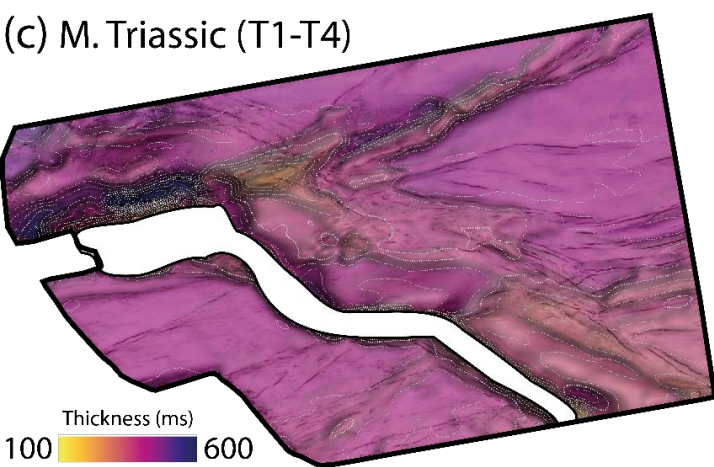
(a) Paleozoic (T8-P-C6)



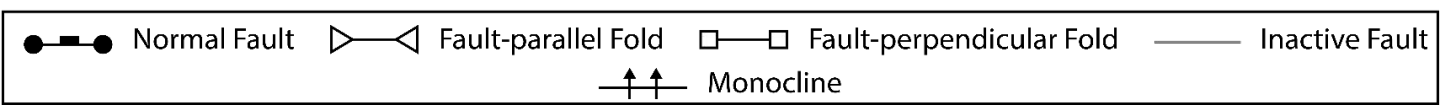
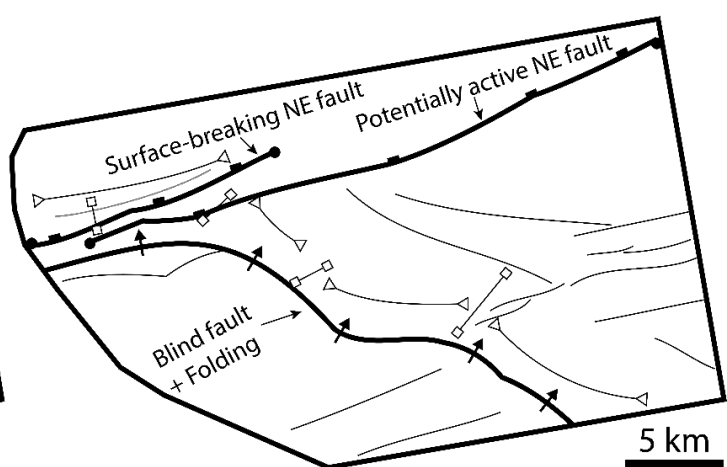
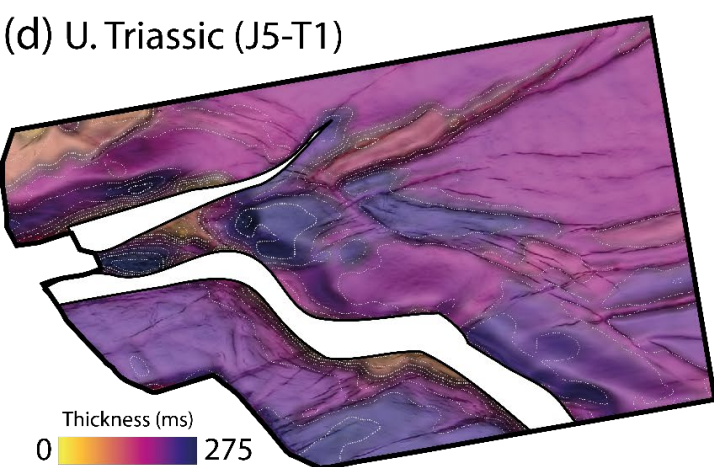
(b) L. Triassic (T4-T8)



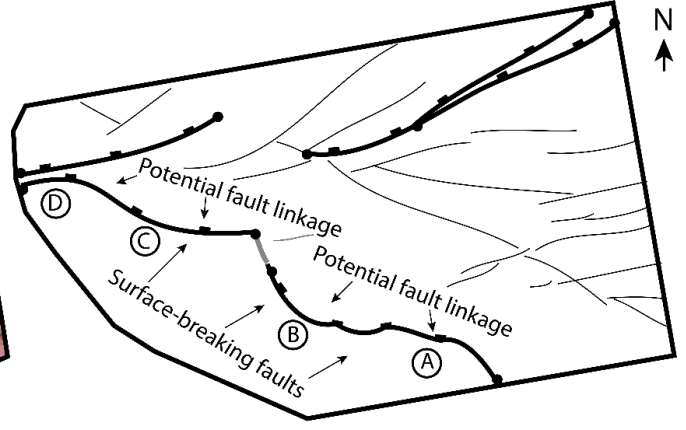
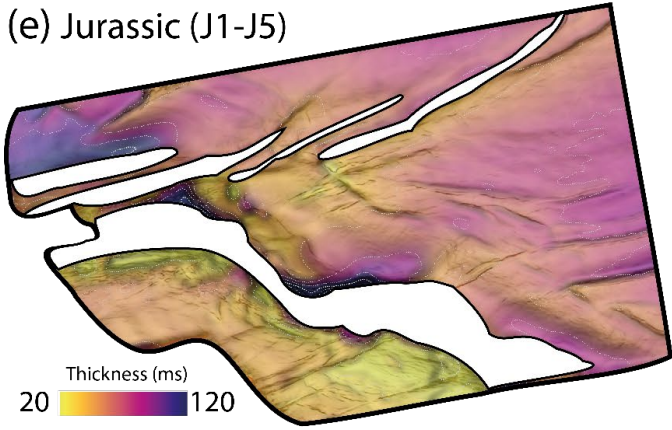
(c) M. Triassic (T1-T4)



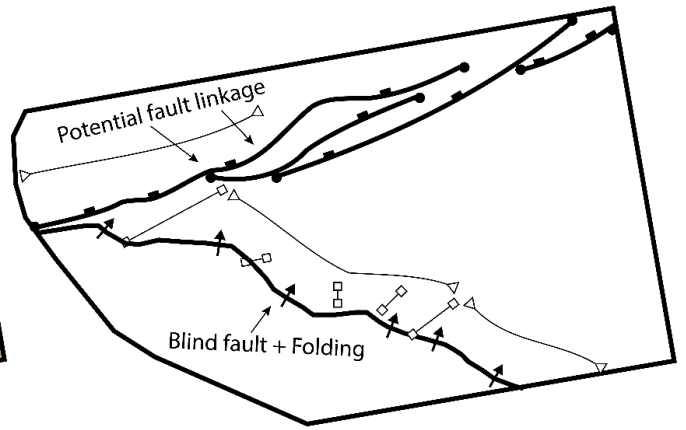
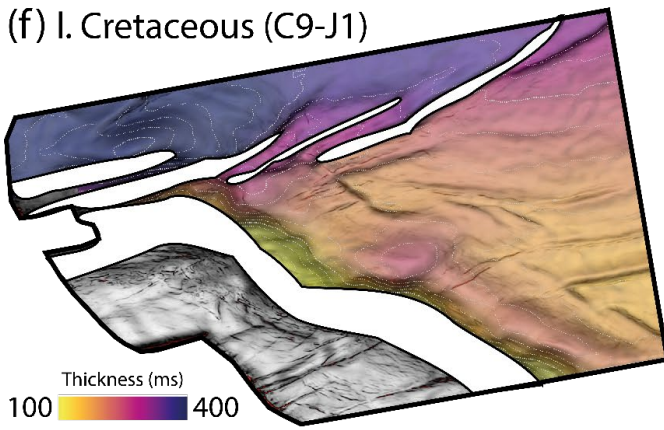
(d) U. Triassic (J5-T1)



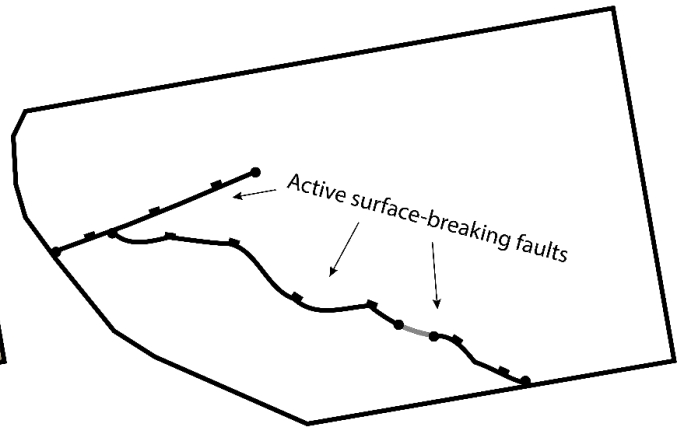
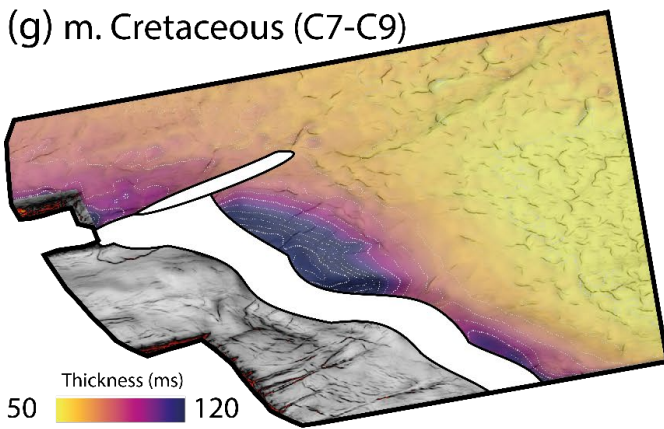
(e) Jurassic (J1-J5)



(f) l. Cretaceous (C9-J1)



(g) m. Cretaceous (C7-C9)



(h) u. Cretaceous (P3-C7)

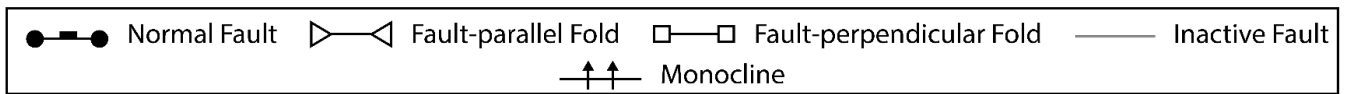
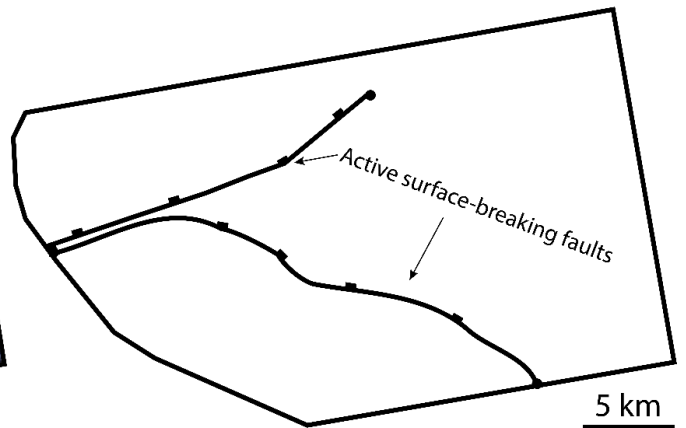
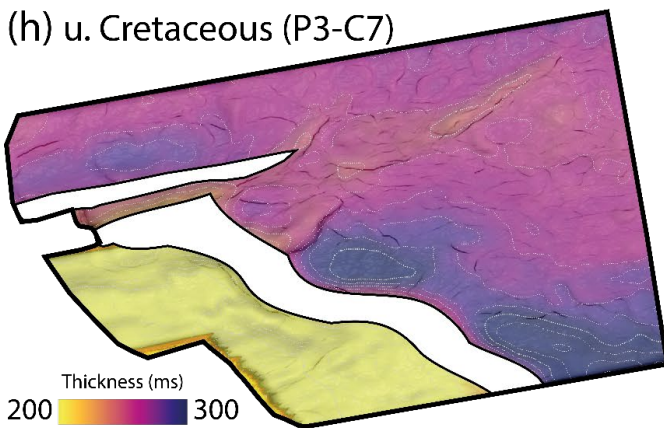


Figure 10. Isochrone maps superimposed on variance attribute surfaces (left) and interpretive sketches (right) for key stratigraphic units across the TFFC. The isochrone maps and accompanying sketches illustrate the thickness variations across the stratigraphic unit and constrain the timing of fault activity in the TFFC and adjacent faults. The location of individual TFFC fault segments is marked by the labelled circles A – D.

1 **Seismic well tie workflow**

2 In this study, we have a 3D seismic reflection survey and one wellbore. The wellbore has available
3 wireline logs that include density and sonic logs that can be used for seismic well tie. The sonic
4 log data cover a depth interval of c.440 m to total depth (2730 m). While the density log data
5 were measured from c. 1200 m to c. 2700 m (Fig 2). However, the wellbore data did not include
6 any checkshot data or a time depth relationship. Therefore, we followed the workflow described
7 next to establish a time depth relationship between the wellbore and seismic reflection data at
8 the well location.

9 The first step we did was to interpret key horizons in our seismic data that marked major changes
10 in seismic facies or character. On this step, the horizon interpretation was done on a 64x64 grid
11 (in-line, cross-line spacing), which was followed by 3D auto-tracking. This was followed by manual
12 edits on complex areas or areas that the auto-tracking did not perform well. Next, we performed
13 a qualitative seismic stratigraphic correlation with offset wells from nearby studies, where we
14 tried to correlate major seismic units based on their overall attributes (i.e., amplitude strength,
15 frequency, lateral continuity and geometry of reflectors). These studies are Harishidayat et al.
16 (2015), Mohammedyasin et al. (2016) and Torabi et al. (2019). Wellbore 7125/4-2 used in
17 Harishidayat et al. (2015) and Torabi et al. (2019) is located c. 34 km SE of our study area while
18 wellbore 7121/4-1 from Mohammedyasin (2016) is situated c. 104 km away towards the west.
19 Representative seismic sections used for this correlation are shown in Fig 3.

20

21 After establishing a seismic stratigraphic correlation with offset wells, we proceeded to
22 determine a time-depth relationship at the wellbore location in our study area and calculate a
23 pseudo seismic velocity log. This served as a first iteration towards constraining the age
24 relationships in our study area and reaching a reliable seismic-well tie. We only used this pseudo
25 velocity log as a comparative measure for other velocity estimates to make sure that we are using
26 reasonable values and not completely off with our estimations. The second step we took was to
27 generate a simplified layer cake velocity model using our key seismic surfaces that represented
28 the top of each key seismic unit along with interval velocity values calculated from the average
29 sonic log response the corresponds with each seismic unit. Where sonic log data are missing, we
30 used geologically reasonable seismic velocity estimates that accounted for lithology and depth.
31 From this velocity model, we derived a second time-depth relationship. We also calculated a third
32 time-depth relationship using the previous approach but after applying a median filter to the
33 sonic log data to remove any outlier data points. Together, these velocity modelling steps
34 resulted in two time-depth relationships that we later used as pseudo checkshot data in the
35 seismic-well tie process together with a reference time-depth relationship that was calculated
36 from offset wells and used as a quality check measure.

37 We followed a two-step workflow to perform the seismic-well tie at the wellbore location in our
38 study area. First, we applied a median filter to the density log data to remove any spikes or outlier
39 data points. Then, we used the filtered density and sonic logs to generate a synthetic
40 seismogram, which we combined with the time-depth relationship (derived from the filtered
41 sonic log data) to tie the well tops to the seismic data. Given the limited coverage of the density
42 log compared to the sonic log, this seismic-well tie step could only tie the well tops from c. 1200

43 m (Top Hekkingen Formation) to c. 2600 m (Top Havert Formation). Nonetheless, this was a
44 useful step to get a more accurate time-depth relationship that is well-constrained for those
45 deeper horizons. The second step in our efforts to get a reliable seismic-well tie at our area of
46 interest was to use the time-depth relationship from the last step and combine it with a synthetic
47 seismogram that was generated from sonic log data and a computed density log using sonic log
48 data to perform a final seismic-well tie. This newly generated synthetic seismogram can be used
49 to tie the shallower well tops (c. 440 m) in addition to the deeper well tops that were covered by
50 the first seismic-well tie step.

51 As a result of this iterative velocity modelling and seismic-well tie method, we were able to tie all
52 available well tops to our seismic data using a well-constrained time-depth relationship that
53 integrates all available data. Lastly, to close the loop and increase our confidence with the
54 seismic-well tie, we compared the final seismic-well tie results that were derived completely from
55 our available data to offset wells from the nearby studies.

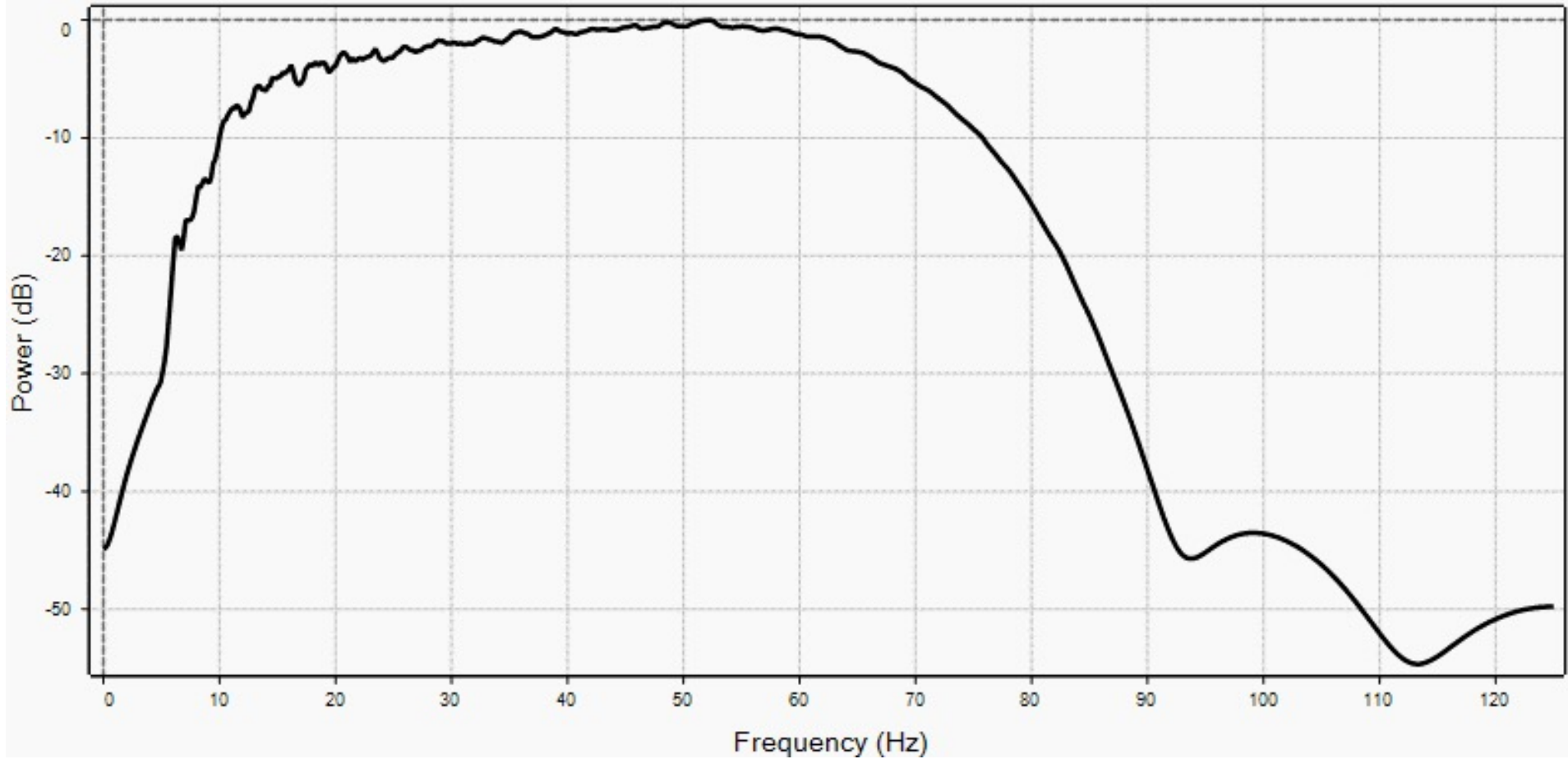


Figure 1. Frequency spectrum for the 3D seismic reflection dataset used in this study. The figure shows that the dominant frequency ranges between 40 – 60 Hz depending on the depth interval within the seismic survey.

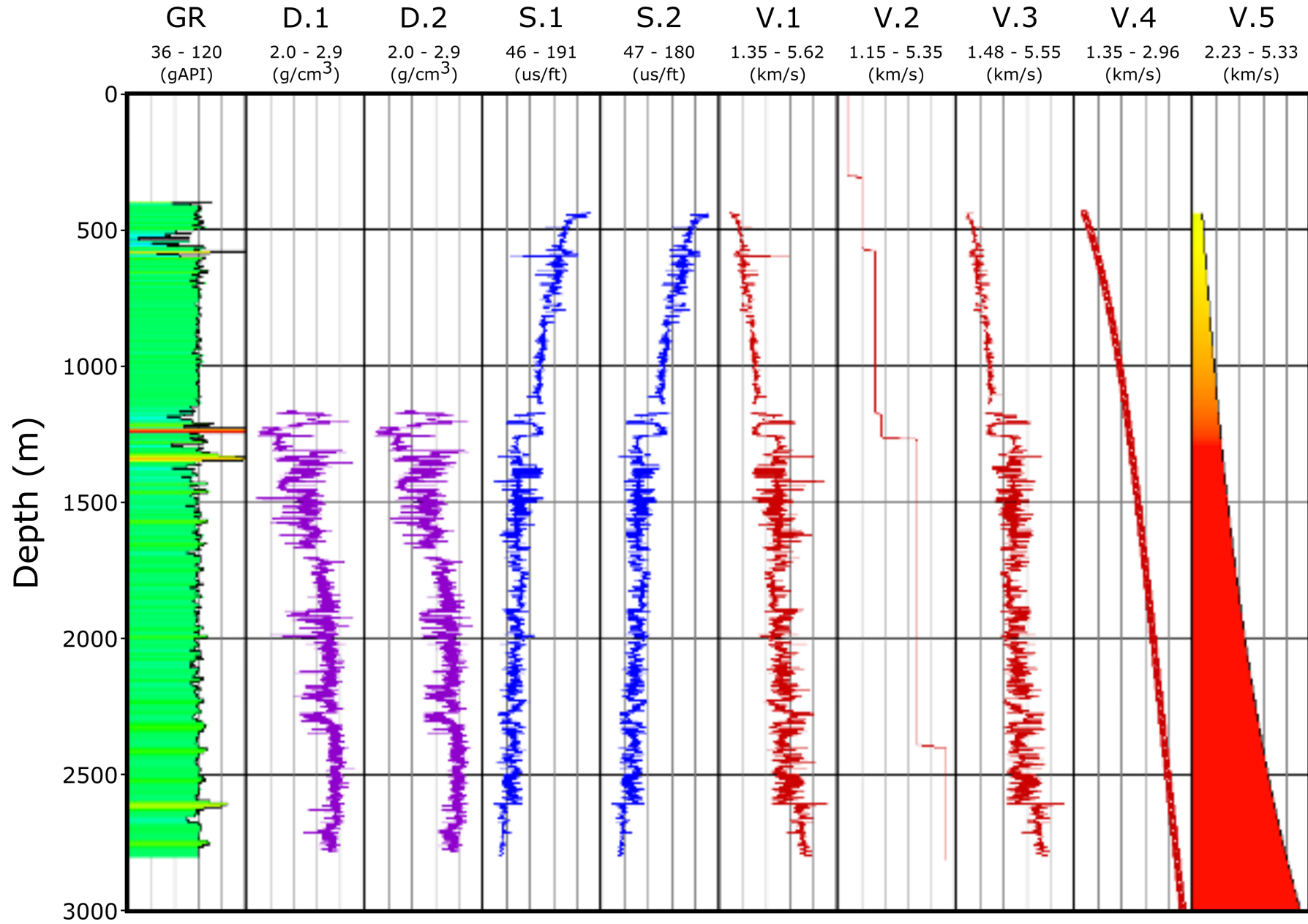
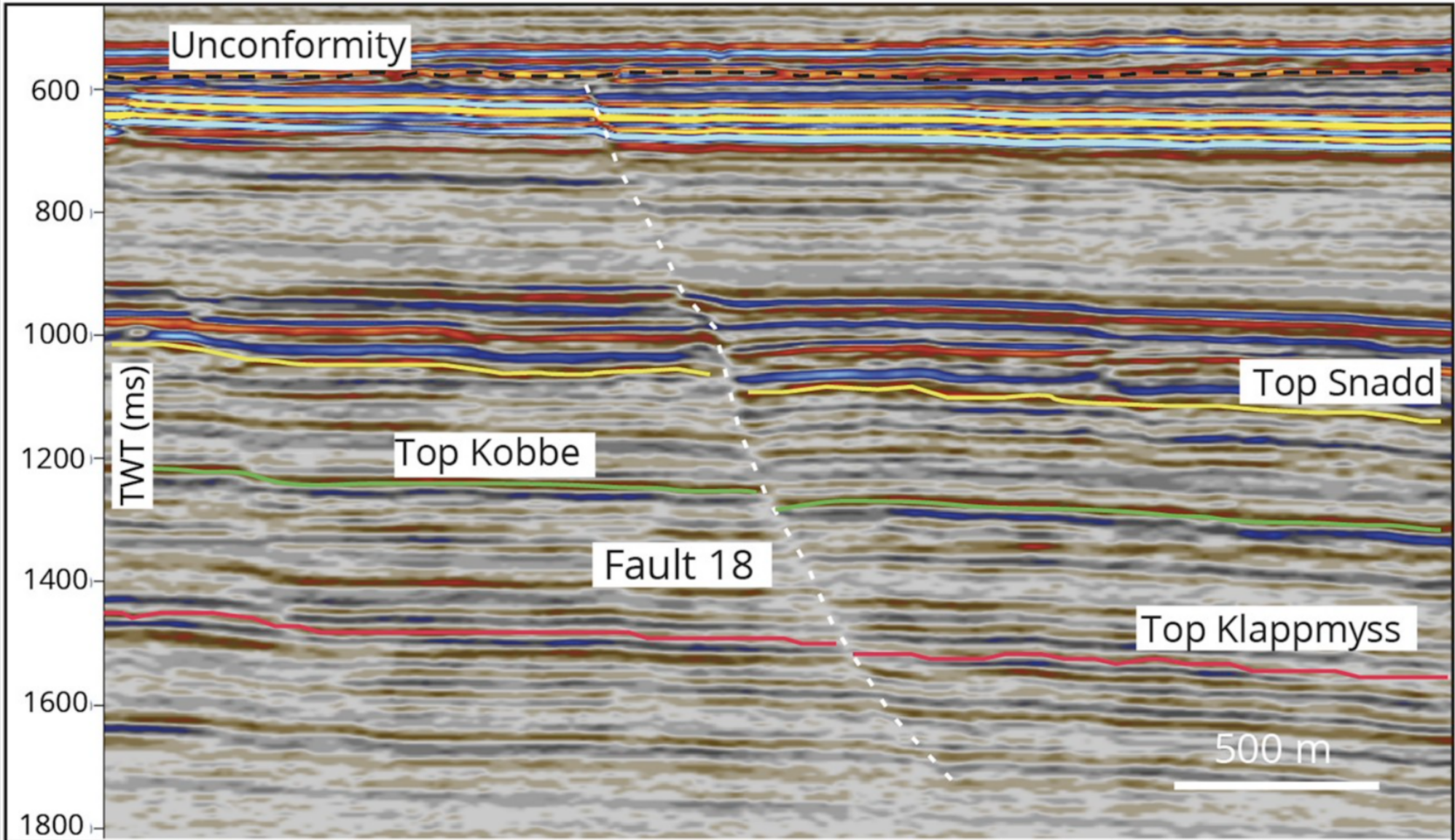
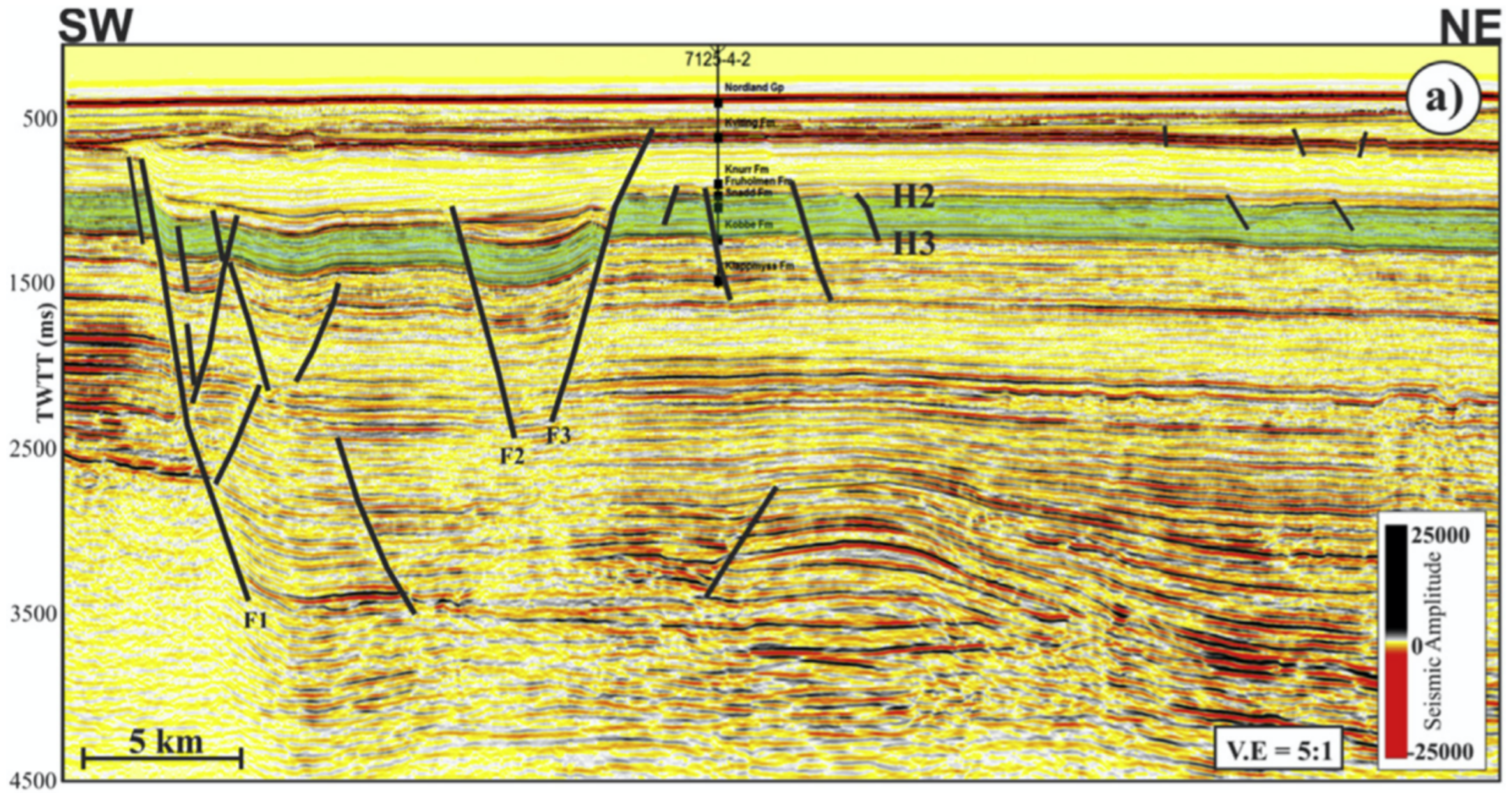


Figure 2. Well section view showing wireline and calculated logs for wellbore 7124/4-1S. The displayed data are for gamma ray (GR), density log (D.1), filtered density log (D.2), sonic log (S.1), filtered sonic log (S.2), calculated velocity from sonic log (V.1), modelled interval velocity using simplified geological model (V.2), calculated velocity from filtered sonic log (V.3), calculated average velocity using estimated time-depth relationship from first seismic well tie (V.4), calculated pseudo interval velocity using estimated time-depth relationship from second seismic well tie (V.5).

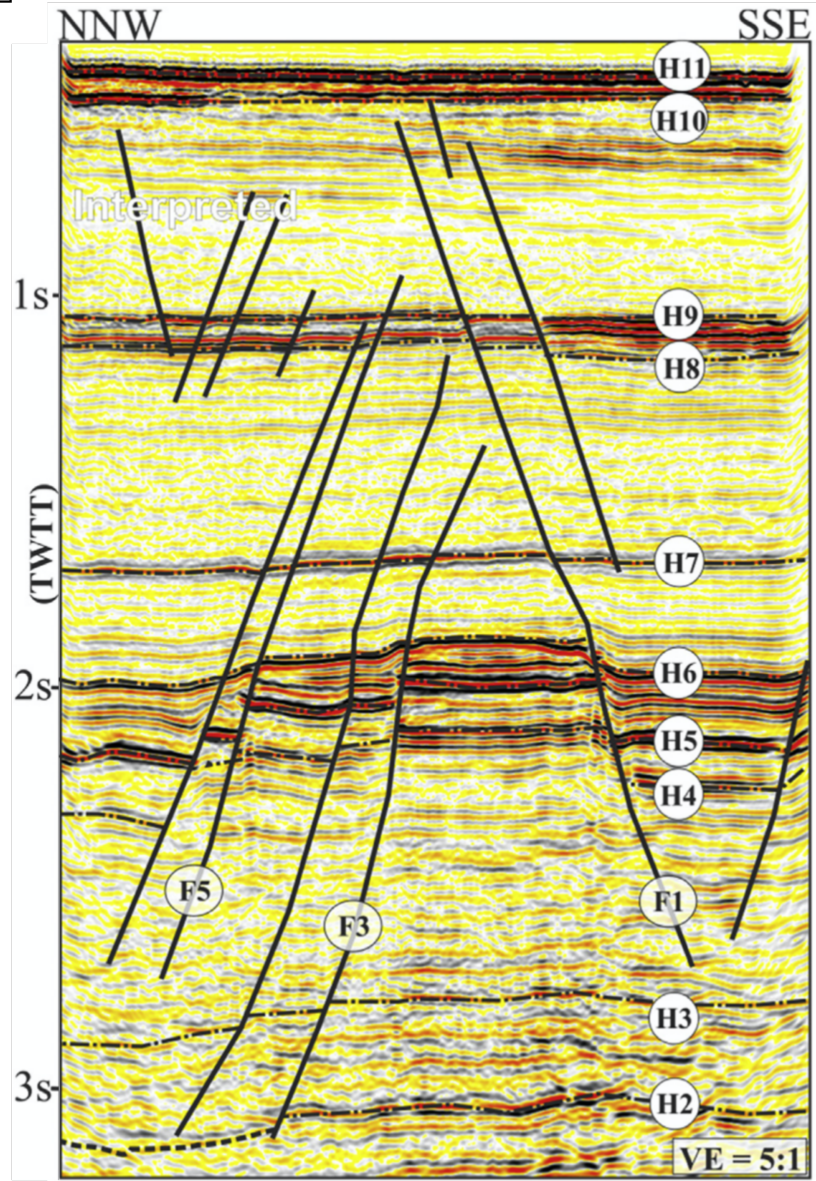
A



B



C



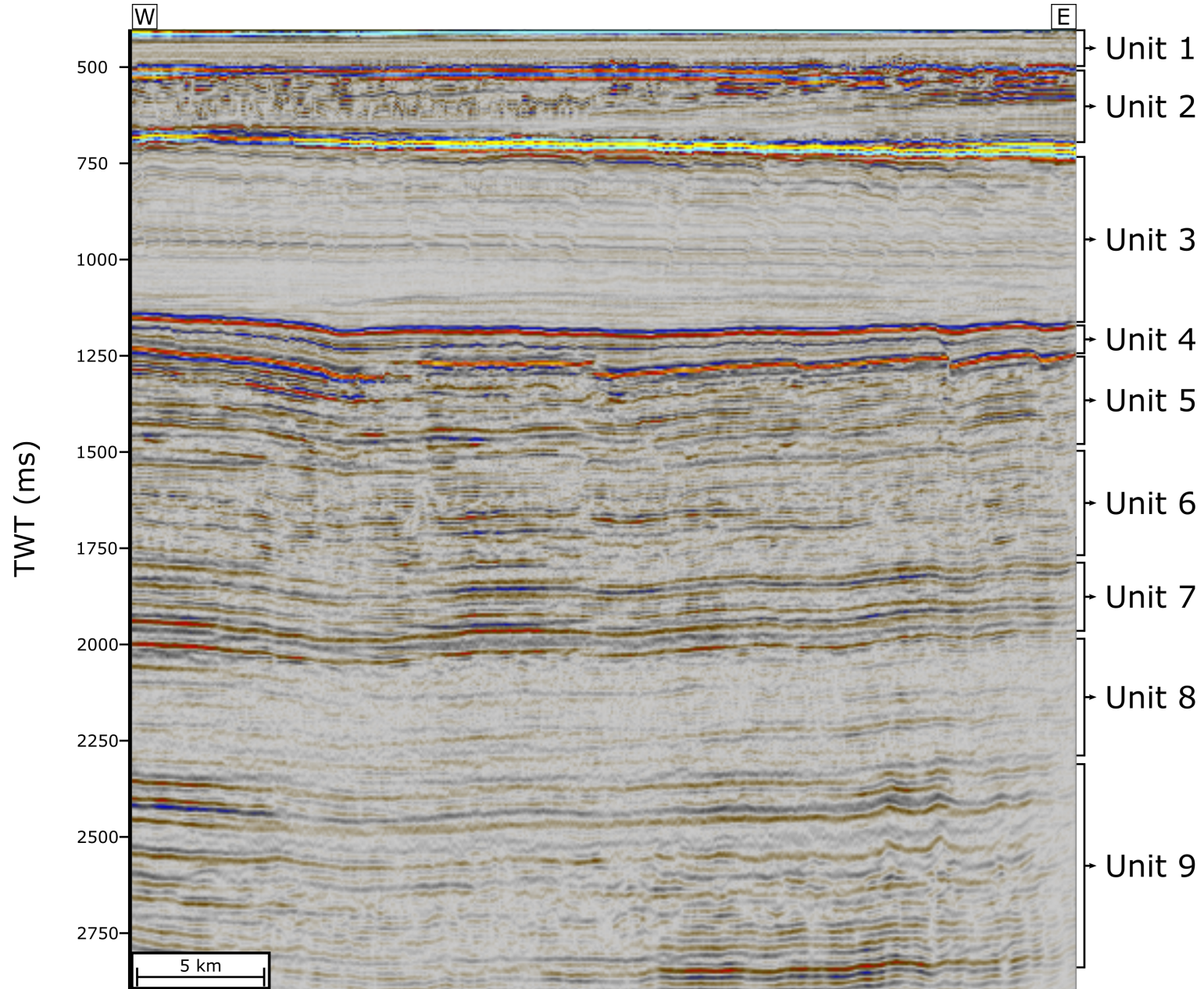
D

Figure 3. Representative seismic sections used for qualitative seismic stratigraphic correlation with offset well (A: Torabi et al., 2019; B: Harishidayat et al., 2015; C: Mohammedyasin et al., 2016; D: our study area).

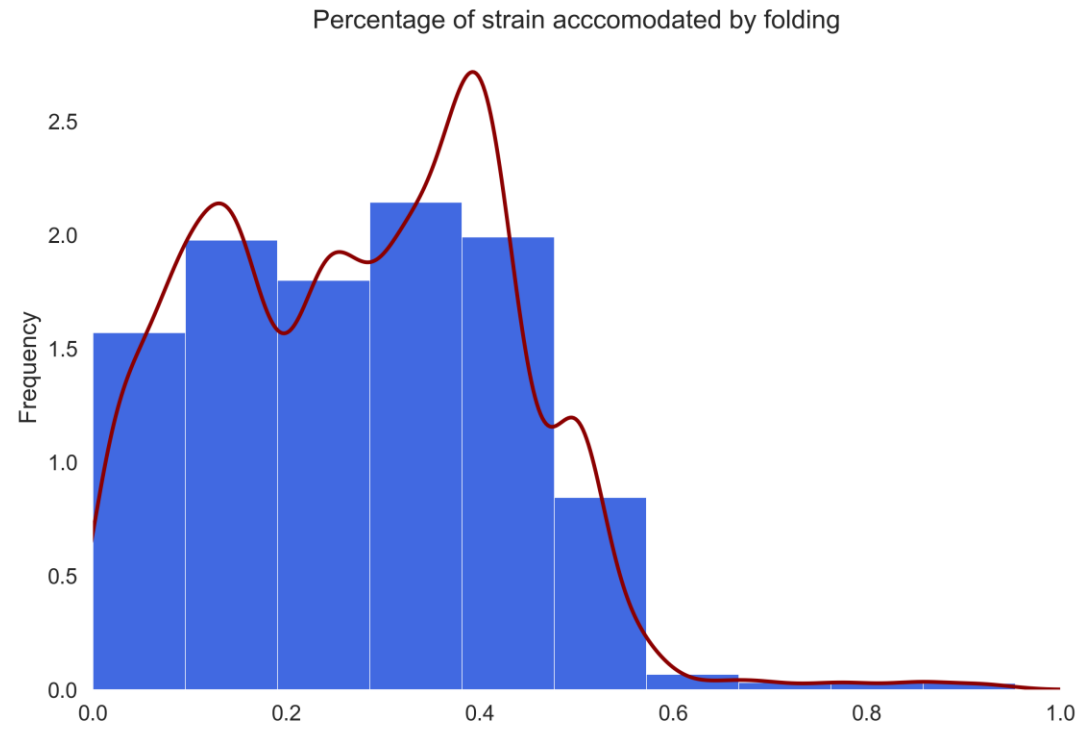


Figure 4. A histogram showing the distribution of strain accommodated by folding. The plot shows that 10 – 40% of total extensional strain is accommodated by the formation of fault-parallel and fault-perpendicular folding.